Numerical Investigation of Roughness Effects on Transition on Spherical Capsules

Stefan Hein* and Alexander Theiss†
German Aerospace Center (DLR), 37073 Göttingen, Germany

Antonio Di Giovanni‡ and Christian Stemmer§
Technical University of Munich, 85748 Garching, Germany

Thomas Schilden¶ and Wolfgang Schröder‖
RWTH Aachen University, 52062 Aachen, Germany

Pedro Paredes,** Meelan M. Choudhari,†† and Fei Li‡‡
NASA Langley Research Center, Hampton, VA 23681

Eli Reshotko§§
Case Western Reserve University, Cleveland, OH 44106

To address the hitherto unknown mechanism of boundary-layer transition on blunt reentry capsules, the role of roughness-induced disturbance growth on a spherical-section forebody is assessed via optimal transient growth theory and direct numerical simulations (DNS). Optimal transient-growth studies have been performed for the blunt capsule experiments at Mach 5.9 in the Hypersonic Ludwieg tube Braunschweig (HLB) of the Technische Universität Braunschweig, which included measurements behind a patch of controlled, distributed micron-sized surface roughness. Transient-growth results for the HLB capsule indicate similar trends as the corresponding numerical data for a Mach 6 experiment in the Actively Controlled Expansion (ACE) facility of the Texas A&M University (TAMU) at a lower Reynolds number. Both configurations indicate a similar dependence on surface temperature ratio, and more important, rather low values of maximum energy gain. DNS are performed for the conditions of the HLB experiment to understand the generation of stationary disturbances by the roughness patch and the accompanying evolution of unsteady perturbations. However, no evidence of either modal or nonmodal disturbance growth in the wake of the roughness patch is found in the DNS

*Research Scientist, Institute of Aerodynamics and Flow Technology, Bunsenstr. 10
†Research Scientist, Institute of Aerodynamics and Flow Technology, Bunsenstr. 10
‡Ph.D. Candidate, Chair of Aerodynamics and Fluid Mechanics, Boltzmannstr. 15
§Privatdozent, Adjunct Teaching Professor, Chair of Aerodynamics and Fluid Mechanics, Boltzmannstr. 15
¶Research Scientist, Institute of Aerodynamics, Wüllnerstr. 5a
‖Head, Institute of Aerodynamics, Wüllnerstr. 5a, AIAA Member
**NASA NPP Fellow, Computational AeroSciences Branch. AIAA Member
††Research Scientist, Computational AeroSciences Branch. AIAA Associate Fellow
‡‡Research Scientist, Computational AeroSciences Branch
§§Kent H. Smith Professor Emeritus of Engineering. Fellow AIAA

data; thus, the physical mechanism underlying the observed onset of transition still remains unknown.

Nomenclature

c	=	damping function
c_T	=	power-law exponent
d	=	Cartesian cell length
f_i	=	disturbance frequency for unsteady computations
$g(\xi, \zeta, \eta, t)$	=	generic flow variable
k	=	peak-to-valley roughness height
h_t	=	total enthalpy
$h_\xi,\ h_\zeta$	=	streamwise and azimuthal metric factors, respectively
m_ζ	=	nondimensional azimuthal wavenumber
$m,\ n$	=	time and space indices in the spatiotemporal analysis, respectively
p	=	pressure
$\overline{\mathbf{q}}$	=	basic flow vector
$\tilde{\mathbf{q}}$	=	unsteady perturbation vector
$\hat{\mathbf{q}}$	=	vector of amplitude functions
r_b	=	local radius
$s, \hat{s}$	=	streamwise coordinate with reference to the stagnation point
t	=	time
(u, v, w)	=	velocity components along streamwise, azimuthal, and wall-normal directions
$A_{m,n}(\xi)$	=	amplitude of the spatiotemporal mode
D	=	face diameter
E	=	energy norm based on total energy
G	=	energy gain
$G_{m,n}(\xi, \eta)$	=	azimuthal wavenumber-frequency spectra
J	=	objective function
K	=	energy norm based on kinetic energy
L	=	twice the edge length of a roughness element
Ma	=	Mach number
$M,\ N$	=	number of time and space samples, respectively

N_E, N_K	=	N-factor, i.e., integrated logarithmic amplification factor, based on E and K, respectively
R	=	face radius
R_a	=	surface mean roughness
R_s	=	spherical-segment radius
Re_{δ^*}	=	Reynolds number based on displacement thickness and flow conditions at boundary-layer edge, $\bar{\rho}_e \bar{u}_e \delta^* / \bar{\mu}_e$
Re_θ	=	Reynolds number based on boundary-layer momentum thickness, $\bar{\rho}_e \bar{u}_e \theta / \bar{\mu}_e$
Re_{kk}	=	roughness Reynolds number based on roughness height and flow conditions at this height, $\bar{\rho}_k \bar{u}_k k / \bar{\mu}_k$
Re_k	=	roughness Reynolds number with dynamic viscosity evaluated at wall temperature, $\bar{\rho}_k \bar{u}_k k / \bar{\mu}_w$
Re_R	=	freestream Reynolds number based on capsule-face radius
Re/l	=	freestream unit Reynolds number
T	=	temperature
$\hat{U}_m(\xi, \zeta, \eta)$	=	time Fourier transform of the streamwise velocity
β	=	dimensional azimuthal wavenumber
γ	=	ratio of specific heats
δ	=	boundary-layer thickness
δ^*	=	boundary-layer displacement thickness
(ξ, ζ, η)	=	streamwise, azimuthal, and wall-normal coordinates
θ	=	boundary-layer momentum thickness
κ_ξ	=	streamwise curvature
λ	=	azimuthal wavelength
μ	=	dynamic viscosity
ρ	=	density
ϕ	=	angular coordinate
χ	=	inclination of the local tangent to the body surface
A, **B**, **C**, **D**, **L**	=	PSE matrix operators
M	=	energy weight matrix

Subscripts

$()_0$	=	inlet disturbance location
$()_1$	=	outlet disturbance location
$()_e$	=	value at the boundary-layer edge
$()_k$	=	value at the roughness height
$()_L$	=	left adjacent cell

$()_R$ = right adjacent cell

$()_w$ = value at the wall

$()_{opt}$ = optimal value

$()_{tr}$ = transition location

$()_\infty$ = freestream value

Superscripts

$()^{mean}$ = mean energy gain

$()^{out}$ = outlet energy gain

$()^\dagger$ = adjoint

$()^H$ = conjugate transpose

I. Introduction

Vehicles flying at hypersonic Mach numbers are exposed to a significant amount of heat load, and thus, often require a thermal protection system (TPS). Since heat transfer rates of a turbulent boundary layer are much higher compared to the laminar state, the location of laminar-turbulent transition is a crucial design parameter for the TPS. The mechanisms of laminar-turbulent transition on the windward side of blunt bodies like reentry capsules are not well understood so far. However, experiments have shown that surface roughness plays an important role during the transition process [1, 2]. Based on systematic studies of the roughness effects on blunt-body transition, different empirical correlations have been proposed in the literature [3, 4].

Blunt reentry capsules with a sphere-cone shaped forebody like the Mars Science Laboratory (MSL) support modal growth of boundary-layer instabilities on the conical part of the heat shield strong enough to trigger laminar-turbulent transition [5–7]. Configurations where the forebody consists of a spherical segment only, like the Apollo capsule or the Orion Crew Exploration Vehicle (CEV), require a much higher Reynolds number for the onset of modal disturbance growth [8]. Owing to the strong bow shock, the boundary-layer edge Mach number remains subsonic or slightly supersonic on the spherical heat shield, which excludes the possibility of second-mode amplification. Due to the spherical body shape, there is a sustained, strongly favorable pressure gradient that has a highly stabilizing effect on the first-mode instabilities. Moreover, although the flow is strongly accelerated, the crossflow velocity component inside the boundary layer remains small because of the weak curvature of the boundary-layer edge streamlines. Therefore, crossflow-mode amplification is not relevant either, and the Görtler-type instability is precluded due to the convex surface curvature. Nevertheless, laminar-turbulent transition is observed on such configurations, even at Reynolds numbers for which, according to the linear stability theory, no modal disturbance growth can be found. This phenomenon is denoted as “blunt-body paradox” in the literature [9].

In situations where the flow does not support modal disturbance amplification, transient growth is still a possible scenario for significant disturbance growth [10]. Basically, a linear superposition of modal disturbances may exhibit transient growth in amplitude despite the fact that each individual mode is decaying in the downstream direction. The transient amplification becomes possible only because the individual modes are nonorthogonal to each other, which is a consequence of the non-normality of the underlying governing equations. The overall nonmodal growth strongly depends on the initial shape of the disturbance. Therefore, an optimization procedure is typically used to identify the optimal initial condition that leads to the maximum transient growth, excluding the question of a physical realizability of the initial disturbance. Hence, such optimal transient-growth studies provide an upper limit on the nonmodal disturbance growth.

Transient disturbance growth has been proposed in literature as a possible cause for laminar-turbulent transition, in particular for those cases where modal disturbance amplification is too weak. Reshotko & Tumin [11] considered nosetip transition and used optimal transient-growth results to derive a correlation for roughness-induced transition in the near vicinity of the stagnation point of blunt geometries. Their correlation uses the same parameters as these purely empirical correlations [3, 4], which relate the momentum thickness Reynolds number at the transition-onset location with the surface-roughness height and the ratio of surface to boundary-layer edge temperatures. However, the exponents describing the roughness and surface temperature effects are derived from physical considerations together with optimal transient-growth theory. The correlation of Reshotko & Tumin will be denoted as "RT-correlation" from here on. The RT-correlation was able to reproduce the trends of the various data sets used to derive the empirical correlations. However, the optimal transient-growth approach of Reshotko & Tumin included some simplifying assumptions. Therefore, Paredes et al. [12] used an improved framework of optimal transient-growth analysis that removed the shortcomings of the approach of Reshotko & Tumin and applied it to the scale model of the Orion CEV geometry studied in the Mach 6 ACE wind tunnel at Texas A&M University (TAMU) [13, 14]. In these experiments, the effect of uniformly-distributed surface roughness on transition onset was systematically studied. For the comparatively small Reynolds numbers considered in this experiment, the necessary roughness height to trigger transition in the stagnation flow region was in the order of 0.7 to 1.5 boundary-layer thicknesses [14]. Despite the significant effects of the nonsimilar boundary layer on the transient-growth characteristics, Paredes et al. found that the transient-growth scaling with respect to Reynolds number and the ratio of surface to edge temperature did not change significantly after the improved framework was applied. Since the RT-correlation depends only on those two scalings, the modified correlation remained close to the original correlation of Reshotko & Tumin despite the improvements in the calculation of optimal growth factors. Paredes et al. [12] also pointed out that the magnitude of transient growth up to the measured transition locations at the experiments at TAMU was rather small, which raises questions regarding the relevance of the optimal growth paradigm.

Additional experimental studies [8, 15, 16] on laminar-turbulent transition in the boundary layer of a blunt Apollo-like

capsule were performed at Mach 5.9 in the Hypersonic Ludwieg tube at the Technische Universität Braunschweig (HLB) in the unit Reynolds number range of $Re/l \approx 6 \times 10^6$ /m to $Re/l \approx 20 \times 10^6$ /m. Infrared (IR) thermography was used to monitor laminar and transitional surface heating. IR measurements based on a standard IR coating with a mean roughness of $R_a \approx 10\,\mu$m revealed the appearance of transitional surface heating at $Re/l \approx 15 \times 10^6$ /m. For a highly polished surface with $R_a \approx 0.5\,\mu$m, no indication of transition was found within the unit Reynolds number range of the HLB. As expected, linear stability analyses for the nominally smooth surface showed that the laminar boundary layer is highly stable. Much larger unit Reynolds numbers would be required for the onset of modal boundary-layer instability growth [8]. Numerical studies on modal disturbance growth in the wake of discrete roughness elements at unit Reynolds number conditions of the experiment showed that roughness element heights well above the mean roughness of the IR coating are required for the onset of a noteworthy modal disturbance growth in the wake flow [17, 18]. For further studies of the distributed surface-roughness effects, a specifically designed micron-sized surface-roughness patch of 20 mm × 20 mm was fabricated and placed at the center of the capsule forebody [16]. The patch consists of uniformly-spaced rectangular micron-sized roughness elements. It features a similar R_a value as the surface with the standard IR coating but has a roughness structure that is well defined, reproducible, and also amenable to numerical studies. The roughness patch triggered laminar-turbulent transition in recent experiments in the HLB at unit Reynolds numbers that are similar to those required in the case of the IR coating. Similar to the experimental results for the standard IR coating, the onset of transition depends on the position of the capsule model in the wind-tunnel test section [16]. If the capsule model with increased roughness height (i.e., either with standard IR coating or with the roughness patch applied) is positioned such that its stagnation point region is located closer to the centerline of the test section, transition is observed for $Re/l \gtrapprox 15 \times 10^6$ /m. In the transitional region, several broadband peaks appear in the hot-wire spectra above 100 kHz. If the stagnation flow region is moved further away from the wind-tunnel centerline, then no transition is observed. Due to peculiar design characteristics of the HLB, the freestream disturbance level near the center is moderately higher than that outside the centerline zone.

One of the main objectives of the present paper is to assess the potential for nonmodal disturbance growth on the forebody of the HLB capsule by using optimal transient-growth theory. Specifically, the effects of surface temperature and unit Reynolds number on the optimal transient growth are investigated and compared with the results for the TAMU capsule at a similar Mach number but lower Reynolds numbers [12]. Furthermore, the steady disturbance flow field introduced by the roughness patch on the HLB capsule and its interaction with additional unsteady disturbances is studied by direct numerical simulations (DNS) in order to investigate possible modal or nonmodal disturbance growth mechanisms either in the vicinity of the roughness patch or in the wake region behind the patch. The different numerical approaches used are briefly introduced in Sec. II and the blunt body configurations considered are described in Sec. III. The optimal transient-growth results for the HLB capsule are presented in Sec. IV and compared to corresponding data for the TAMU capsule. The additional data set for the HLB capsule is used to further substantiate the value of

the power-law exponent of the wall to boundary-layer edge temperature ratio of the correlation for roughness-induced transition that was originally proposed by Reshotko & Tumin [11] and the slightly different value recently derived by Paredes et al. [12] based on optimal transient-growth data for the TAMU capsule. In Sec. V, the results of direct numerical simulations are presented that attempt to replicate the conditions of the HLB capsule experiment with the specifically tailored roughness patch. The experimental results for the HLB and TAMU capsules among others are discussed in further detail in a companion paper by Radespiel et al. [16].

II. Methodologies

This section introduces the different methodologies used in this paper. First, a brief overview of the linear optimal transient-growth theory based on parabolized stability equations is given, where an initial disturbance is sought that maximizes an objective function. The following subsection highlights the methods used for the direct numerical simulation.

A. Optimal Transient-Growth Theory

The optimal transient-growth analysis is performed using the framework of linear parabolized stability equations (PSE) as elucidated in the literature [19–22]. The method is outlined here for the sake of completeness.

1. Governing Equations

In the PSE concept, the stationary three-dimensional disturbance $\tilde{\mathbf{q}}$ can be written as

$$\tilde{\mathbf{q}}(\xi,\zeta,\eta) = \hat{\mathbf{q}}(\xi,\eta)\exp\left(i\beta\zeta\right) + c.c., \tag{1}$$

where $c.c.$ denotes the complex conjugate and $\hat{\mathbf{q}}(\xi,\eta) = \left[\hat{\rho},\hat{u},\hat{v},\hat{w},\hat{T}\right]^T$ represents the vector of amplitude functions, containing the density and temperature fluctuations ($\hat{\rho},\hat{T}$), as well as the velocity disturbances ($\hat{u},\hat{v},\hat{w}$) in the streamwise (ξ), azimuthal (ζ), and wall-normal direction (η), respectively. The wavenumber along the azimuthal (ζ) direction is β and the disturbance azimuthal wavelength is defined as $\lambda\left(\xi\right) = 2\pi/\beta$.

Introducing the perturbation form from Eq. (1) into the linearized Navier-Stokes equations and assuming a slow streamwise variation of the basic state and of the amplitude functions to neglect the viscous derivatives in the streamwise direction, the nonlocal linear stability equations are obtained and can be written in the form

$$\mathbf{L}\hat{\mathbf{q}}(\xi,\eta) = \left(\mathbf{A} + \mathbf{B}\frac{\partial}{\partial\eta} + \mathbf{C}\frac{\partial^2}{\partial\eta^2} + \mathbf{D}\frac{\partial}{\partial\xi}\right)\hat{\mathbf{q}}(\xi,\eta) = 0. \tag{2}$$

The linear operators $\mathbf{A}$, $\mathbf{B}$, $\mathbf{C}$, and $\mathbf{D}$ are provided in Ref. [23] along with a more detailed explanation on the derivation of the PSE. The parabolized stability equations (Eq. (2)) are integrated in the downstream ξ-direction using a marching

procedure. Even though the system has been 'parabolized', some ellipticity remains and information is allowed to propagate upstream, which in turn can cause numerical instabilities if the step size in ξ becomes too small. Chang et al. [24] identified the $\partial\hat{p}/\partial\xi$-term as the most relevant source of remaining ellipticity, however, this term is of higher order for transient-growth problems [25, 26] and, therefore, will be omitted for the present work.

2. Optimality System

In the optimal transient-growth framework, a set of perturbation profiles at an initial location, $\tilde{\mathbf{q}}_{\mathbf{0}} = \tilde{\mathbf{q}}_{\xi_0}$, are sought that maximize a suitably defined objective function, $J(\tilde{\mathbf{q}})$, which is a measure of disturbance energy gain within the optimization interval $[\xi_0, \xi_1]$. There are two definitions of the energy gain that are commonly used for optimal-perturbation problems [19, 22, 27]; namely the outlet energy gain,

$$J = G^{out} = \frac{E(\xi_1)}{E(\xi_0)}, \tag{3}$$

and the mean energy gain,

$$J = G^{mean} = \frac{1}{\xi_1 - \xi_0} \frac{\int_{\xi_0}^{\xi_1} E(\xi')\,\mathrm{d}\xi'}{E(\xi_0)}, \tag{4}$$

where E denotes the energy norm of $\tilde{\mathbf{q}}$. In this work, we use the positive-definite energy norm, proposed by Chu [28], Mack [29], and Hanifi et al. [30], defined as

$$E(\xi) = \frac{1}{\lambda} \int_{\zeta} \int_{\eta} \tilde{\mathbf{q}}(\xi, \zeta, \eta)^H \mathbf{M_E} \tilde{\mathbf{q}}(\xi, \zeta, \eta)\, h_\xi h_\zeta \mathrm{d}\eta \mathrm{d}\zeta, \tag{5}$$

where the superscript H denotes conjugate transpose and h_ξ, h_ζ are metric factors associated with the streamwise and azimuthal curvature, respectively. The total energy weight matrix, $\mathbf{M_E}$, includes all five state variables and is defined by

$$\mathbf{M_E} = \mathrm{diag}\left[\frac{\bar{T}(\xi,\eta)}{\bar{\rho}(\xi,\eta)\,\gamma Ma^2}, \bar{\rho}(\xi,\eta), \bar{\rho}(\xi,\eta), \bar{\rho}(\xi,\eta), \frac{\bar{\rho}(\xi,\eta)}{\gamma(\gamma-1)\,\bar{T}(\xi,\eta)\,Ma^2}\right]. \tag{6}$$

An overbar denotes meanflow quantities, γ is the ratio of specific heats and Ma is the Mach number. Additionally, an energy norm, which is solely based on the kinetic energy of the disturbance is also used in this paper. The energy weight matrix, in this case, reduces to

$$\mathbf{M_K} = \mathrm{diag}\left[0, \bar{\rho}(\xi,\eta), \bar{\rho}(\xi,\eta), \bar{\rho}(\xi,\eta), 0\right]. \tag{7}$$

To distinguish when the objective function is maximized for the total energy E or the kinetic energy K of a disturbance, a corresponding subscript is added to the objective function, resulting in four different possible options: J_E^{out}, J_K^{out},

J_E^{mean}, and J_K^{mean}.

An adjoint-based optimization algorithm is applied to determine the maximum of the objective functional J, employing the intrinsic parabolic nature of the equations. Starting from an initial guess at ξ_0 the direct PSE, $\mathbf{L}\tilde{\mathbf{q}} = 0$, are used to march the solution $\tilde{\mathbf{q}}$ from $\xi = \xi_0$ to $\xi = \xi_1$, where the final optimality condition is used to obtain the initial condition for the backward integration of the adjoint PSE, $\mathbf{L}^\dagger\tilde{\mathbf{q}}^\dagger$ = RHS, where RHS = 0 in case of outlet energy gain optimization (J^{out}) and RHS = $2\mathbf{M}^H\tilde{\mathbf{q}}$ for the mean energy optimization (J^{mean}). A new initial condition for the forward problem is obtained from the adjoint solution at ξ_0 employing the initial optimality condition. The optimization procedure is terminated when the value of J has converged to a prescribed tolerance, which was set to 10^{-4} in the present computations. In this work, we have used the continuous, as well as the discrete adjoint approach for integrating $\tilde{\mathbf{q}}^\dagger$ from ξ_1 to ξ_0, revealing no impact of the adjoint method on the optimal disturbance growth. All results shown in this paper have been computed by applying the continuous adjoint approach.

3. Spatial Discretization and Boundary Conditions

The PSE are discretized with a stable high-order finite-difference scheme (FD-q) [31] of sixth order along the wall-normal direction. The perturbations are integrated along the streamwise coordinate by using second-order backward differentiation and a constant step size. The number of discretization points was varied in both spatial directions to ensure grid convergence of the optimal transient-growth results, whereas clustering of grid points toward the wall was performed. No-slip, isothermal boundary conditions are imposed at the wall, i.e., $\hat{u} = \hat{v} = \hat{w} = \hat{T} = 0$. At the upper boundary, which is located just below the shock layer, homogeneous Dirichlet conditions, $\hat{\rho} = \hat{u} = \hat{v} = \hat{T} = 0$, and a Neumann boundary condition for the wall-normal velocity component, $\hat{w}_\eta = 0$, are prescribed.

4. Cross-Comparison of the Optimal Transient-Growth Codes

The nonmodal disturbance growth results presented in this paper have been computed with two different codes. The optimal-growth framework developed by NASA is used for the computations for the TAMU ACE capsule configuration and has been extensively verified [21]. On the other hand, a newly developed optimal transient-growth code by DLR is employed for characterizing the nonmodal growth properties of the boundary layer on the HLB capsule. A more detailed overview of the two different capsule configurations is given in Sec. III.

The boundary-layer flow over a hemisphere at $Ma = 7.32$ is considered to cross-verify the two different transient-growth implementations used in this work. Details on the basic flow computations by NASA were reported by Li et al. [32], and the nonmodal disturbance growth characteristics of the boundary layer in downstream direction are given in Ref. [22]. Figure 1 depicts the streamwise evolution of basic flow variables at the edge of the boundary layer along the angular coordinate ϕ ($\phi = \xi/R_s$ with R_s being the radius of the hemisphere). The boundary-layer edge is defined as the wall-normal position where the total enthalpy reaches 99.5% of the freestream value ($h_t/h_{t,\infty} = 0.995$). The basic

state computed by DLR uses the numerical framework described in Theiss et al. [8]. Figure 2 shows the optimal outlet energy gain based on the total energy of the disturbance, G_E, at a fixed output location and varying inflow positions as a function of the azimuthal wavenumber, m_ζ, for the basic state computed by DLR. An excellent agreement of the predicted gain from both codes is observed.

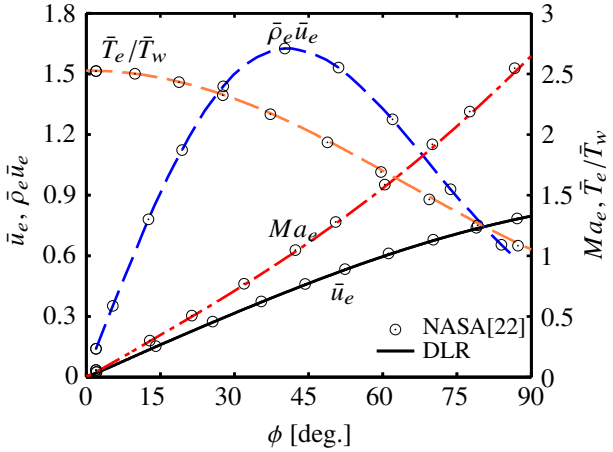

Fig. 1 Streamwise evolution of basic flow variables at the edge of the boundary layer for the hemisphere computed by DLR (lines) and NASA (symbols).

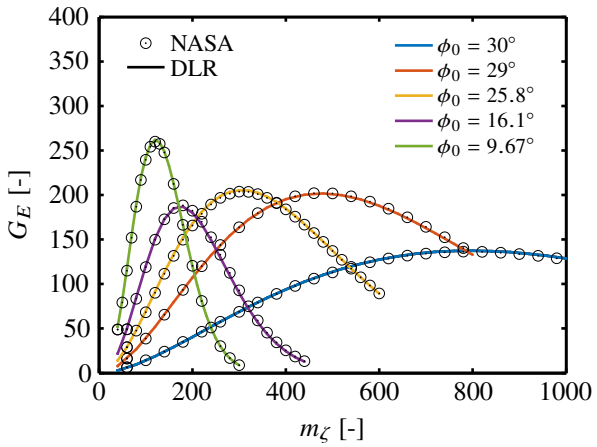

Fig. 2 Total energy gain G_E at $\phi_1 = 32.2°$ optimized for $J = G^{out}$ as a function of the azimuthal wavenumber m_ζ and varying ϕ_0; lines: computations by DLR, symbols: computations by NASA.

B. Direct Numerical Simulations

The numerical method used by RWTH solves the compressible Navier-Stokes equations in space and time [33]. The computational domain is discretized by an unstructured hierarchical Cartesian mesh whose cells are arranged in an octree structure. The domain decomposition for parallel computations is based on the Hilbert space-filling curve and subtree workloads to distribute subtrees of the hierarchical octree of equal loads to processors [34]. The governing equations are integrated using a finite-volume method [35]. The boundaries of the computational domain are embedded in the Cartesian mesh and modeled employing cut cells [33]. Small cut cells are treated using an interpolation and flux-redistribution scheme [35].

For the spatial discretization, an advection upstream splitting method (AUSM) is used. The advection Mach number on the cell surface is the mean of the extrapolated Mach numbers from the adjacent cells $Ma_{1/2} = 0.5\,(Ma_L + Ma_R)$. The same formulation holds for the pressure on the cell surface. The cell-center gradients are computed using a second-order accurate least-squares reconstruction scheme [33]. Shock capturing is achieved by adding additional numerical dissipation at the shock position. The temporal integration is based on a 5-stage second-order accurate Runge-Kutta scheme. For supersonic flows, the code has been employed and validated for the flow past a cone and around a blunt stagnation point probe [36, 37].

The DNS by the Technical University of Munich (TUM) are performed using the Navier Stokes Multi Block solver (NSMB). NSMB is an MPI-parallelized, finite-volume code for structured grids with a wide variety of numerical schemes; and it has been extensively tested in studies of hypersonic flows [38, 39]. The spatial discretization is based on a 4th-order, central difference scheme, whereas a 4th-order Runge-Kutta method is used for time integration. Artificial numerical dissipation is added to capture the shock and to suppress spurious oscillations.

III. Configurations

A. TAMU Capsule

The first configuration for which transient-growth results are presented corresponds to a blunt, spherical-section forebody at 28° angle of incidence with respect to the free stream. The forebody configuration models the Orion CEV capsule geometry [40]. The face diameter is $D = 2R = 0.0762\,\text{m}$ and the remaining dimensions are scaled according to Hollis [40], resulting in a sphere of radius $R_s = 0.09144\,\text{m}$. The flow conditions at Mach 6 match those of a wind-tunnel experiment in the Actively Controlled Expansion (ACE) tunnel at the National Aerothermochemistry Laboratory (NAL) of Texas A&M University [13, 14]. Paredes et al. [12] performed transient growth calculations for four freestream unit Reynolds numbers, namely, $Re/l = 3.4 \times 10^6$ /m, 4.4×10^6 /m, 5.4×10^6 /m, and 6.4×10^6 /m. The freestream temperature was set to $\bar{T}_\infty = 54.69\,\text{K}$ and the surface temperature was equal to $\bar{T}_w = 391.0\,\text{K}$. To investigate the effects of surface temperature on the transient-growth characteristics, computations were also performed for additional, cooler surface temperatures corresponding to $\bar{T}_w = 300.0\,\text{K}$, 195.5 K, and 130.33 K, respectively, with the unit Reynolds number held fixed at $Re/l = 4.4 \times 10^6$ /m.

The basic state, laminar boundary-layer flow over the forebody was computed by using a second-order accurate algorithm as implemented in the finite-volume compressible Navier-Stokes flow solver VULCAN-CFD (see Ref. [41] and http://vulcan-cfd.larc.nasa.gov for further information about the solver). Further details about the laminar basic flow computations are given in Ref. [12].

B. HLB Capsule

The second capsule studied in this work corresponds to an Apollo-shaped capsule with a spherical-section forebody ($D = 0.17\,\text{m}$ and $R_s = 0.204\,\text{m}$) at an angle of attack of AoA = 24°. Laminar basic flow computations are performed for Mach 5.9 freestream conditions that match the experiments of Ali et al. [15] in the Hypersonic Ludwieg Tube at the TU Braunschweig (HLB). Overall, four different unit Reynolds numbers have been computed, namely $Re/l = 10 \times 10^6$ /m, 12.5×10^6 /m, 16×10^6 /m, and 18×10^6 /m with the freestream temperature set to $\bar{T}_\infty = 59.03\,\text{K}$ and prescribed surface temperature of $\bar{T}_w = 295\,\text{K}$. To also assess the impact of surface temperature on the nonmodal disturbance growth characteristics, additional simulations have been performed at fixed freestream conditions for $Re/l = 10 \times 10^6$ /m and modified surface temperatures with $\bar{T}_w = 170\,\text{K}$, 245 K, and 395 K, respectively.

The laminar basic flow was computed with the second-order accurate, three-dimensional, finite-volume, compressible Navier-Stokes flow solver FLOWer [42] on a block-structured grid. More details about the numerical settings and the employed grid are given in Ref. [8].

C. Comparison of Boundary-Layer Edge Data for the Two Capsules

Figure 3 shows a three-dimensional view of the HLB capsule forebody with the Mach number isocontours in the symmetry plane and the Reynolds number based on momentum thickness, Re_θ, on the capsule forebody. Only one half of the model was used in the basic flow computations, exploiting the azimuthal symmetry of the flow field. Due to the strong bow shock, the boundary-layer edge Mach number falls within the subsonic to transonic range and the flow continuously accelerates from the stagnation point at $\xi = 0$ toward the capsule shoulder. In this work, we focus on the leeward symmetry region above the stagnation point, where transition has been observed in experiments [8, 14]. The HLB capsule has been investigated at higher unit Reynolds numbers, and its diameter is about twice the size of the Orion CEV model. The angle of attack differs also, but due to the spherical forebody, the boundary-layer edge values normalized with the respective freestream values are very similar for the two flow configurations as depicted in Fig. 4. In accordance with Sec. II.A.4, the boundary-layer edge is determined from the total enthalpy criterion ($h_t/h_{t,\infty} = 0.995$). For both capsule geometries, the mass flux, $\bar{\rho}_e \bar{u}_e$, increases with growing distance from the stagnation point and reaches its maximum at the sonic point, $Ma_e = 1$, in agreement with the inviscid flow theory.

D. Hemisphere Approximation

To ease the computational effort in the case of unsteady DNS, a reduction of the domain size is performed in the simulations of TUM as shown in Fig. 5. First, the flow over a hemisphere is considered. The flow over the hemisphere well represents the flow over the HLB capsule with angle of attack with minor restrictions outside of the area of interest. Second, results for the laminar steady flow on the whole hemispheric forebody (full domain) are used to generate inflow profiles for a restricted computational domain. The grid resolution of the restricted domain can be increased to match the resolution requirements imposed by the presence of the rough wall.

The steady base flow for the entire hemisphere with smooth surface is computed on an axisymmetric two-dimensional grid. The grid consists of about $76,000$ points clustered around the shock location and inside the boundary layer. To provide similar outflow boundaries as in the case of the reentry capsule, the hemisphere ends with a shoulder resembling the one of the HLB capsule.

For both the 3D capsule and the axisymmetric 2D hemisphere, boundary-layer streamwise velocity and temperature profiles at different positions are shown in Fig. 6 for a unit Reynolds number of $Re/l = 18 \times 10^6\ /m$. The profiles on the 3D capsule geometry are extracted along the symmetry plane. A clear match of the profiles is observed for the two configurations. In particular, the equivalence of the two flows is obtained by comparing velocity and temperature

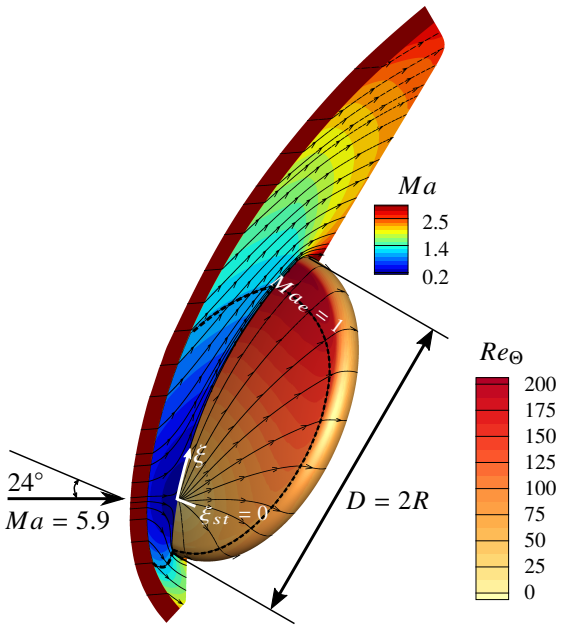

Fig. 3 Three-dimensional view of the HLB capsule forebody with isocontours of Mach number and streamlines along the symmetry plane and contours of Reynolds number based on momentum thickness with boundary-layer edge streamlines on the forebody for $Re/l = 10 \times 10^6$ /m and $\bar{T}_w = 295$ K. The thick dashed lines indicate the sonic lines.

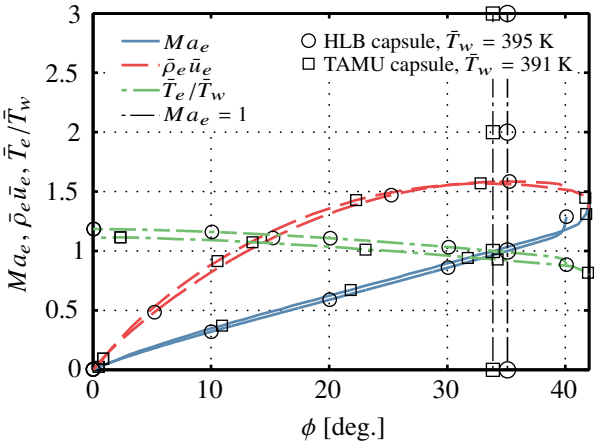

Fig. 4 Streamwise evolution of boundary-layer edge quantities along the symmetry plane for ∘: HLB capsule at $Re/l = 10 \times 10^6$ /m and $\bar{T}_w = 395$ K, □: TAMU capsule at $Re/l = 4.4 \times 10^6$ /m and $\bar{T}_w = 391$ K.

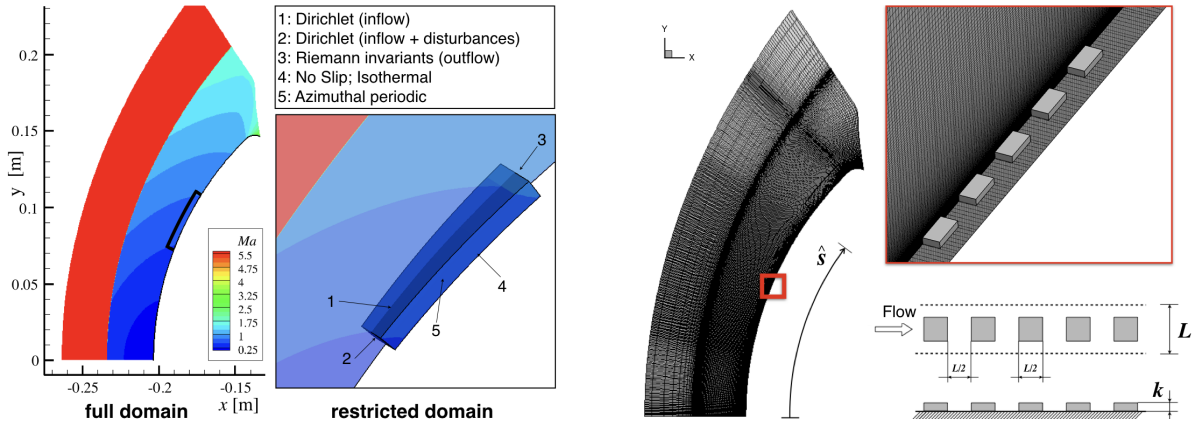

Fig. 5 Representation of the simulation domains with the specified boundary conditions (left) and computational grid with close-up on the roughness position (right). Simulations for the smooth configuration are conducted on the entire hemisphere (full domain), whereas simulations for roughness investigations are conducted on a restricted domain. The box in the left figure shows the position of the restricted domain. The roughness position is indicated by the red square in the right figure.

profiles on the capsule at a given position s with the ones on the hemisphere at $\hat{s} = s + \Delta s$, with s and $\hat{s}$ being the streamwise coordinates on the two geometries with origin on the respective stagnation points. On the capsule, the distance between the stagnation point and the rotation axis is $s = 60.5$ mm. In the vicinity of this position, the flow

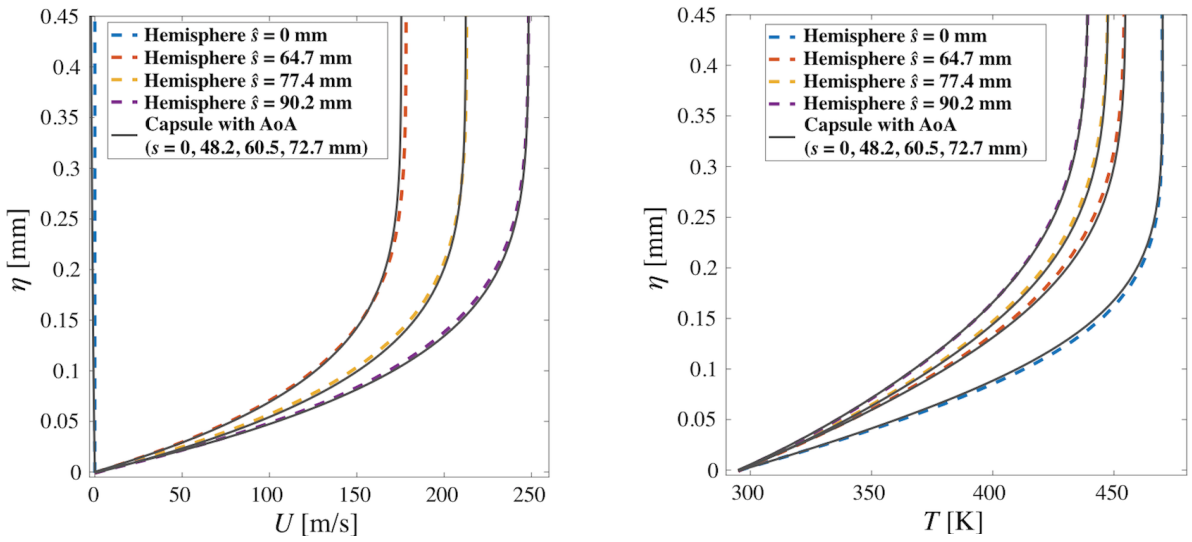

Fig. 6 Comparison of boundary-layer velocity (left) and temperature (right) profiles for the smooth hemisphere and the HLB capsule geometry with AoA = 24°. The origin of the streamwise coordinates s and $\hat{s}$ is set on the stagnation point of the respective configuration.

corresponds to the one on the hemisphere at $\hat{s} = 77.4$ mm. Details on the restricted domains and further comparisons between the capsule and the hemisphere boundary layer in presence of roughness are discussed in Sec. V.B.1.

IV. Results on Optimal Transient Growth

Optimal transient-growth results are presented for the HLB capsule with an emphasis on the effects of unit Reynolds number and wall temperature on the nonmodal growth characteristics and optimal optimization parameters, namely, spanwise wavelength and optimization interval length. For each parametric study, the transient-growth characteristics will be compared to the findings for the TAMU capsule presented in Ref. [12]. Subsequently, the implications of optimal growth results on the transition correlation of Reshotko & Tumin [11] and Paredes et al. [12] are investigated.

In this work, we assume that the spanwise disturbance wavelength, λ (ξ), increases in proportion to the distance from the stagnation point. This ensures a constant wavenumber in the azimuthal direction, m_ζ, at each streamwise position, as it was also used in the axisymmetric case for the hemisphere in Sec. II.A.4. Note that the dimensional spanwise wavenumber β of Eq. (1) turns into the nondimensional, azimuthal wavenumber m_ζ. However, this assumption may not hold for the fully three-dimensional flows investigated in this work. In general, a physically accurate specification of azimuthal-wavenumber variation along a prescribed trajectory in a fully three-dimensional flow remains an open question in the literature for both, modal and nonmodal disturbance growth. For the TAMU capsule, Paredes et al. [12] have examined the effect of different strategies for specifying the streamwise variation in spanwise disturbance wavelength on the transient-growth characteristics for the boundary layer along the leeward line of symmetry. In their

study, the authors tested a constant wavelength approach, a variation based on streamline divergence, and the assumption of axisymmetric flow. Their calculations revealed only a minor impact of the chosen wavelength variation on the optimal transient growth across the optimization interval that led to the highest gain. The assumption of axisymmetric flow for the azimuthal-wavelength variation resulted in the strongest growth of disturbance energy, and hence, can be considered as the strategy that provides the upper bound for nonmodal disturbance growth on the geometries regarded in this work. Under the assumption of axisymmetric flow, the metric factors yield in

$$h_\xi = 1 + \kappa_\xi \eta, \tag{8}$$

$$h_\zeta = r_b + \eta \cos(\chi), \tag{9}$$

where κ_ξ denotes the streamwise curvature ($\kappa_\xi = 1/R_s$), r_b is the local radius ($r_b = R_s \sin(\phi)$), and χ specifies the inclination of the local tangent to the body surface ($\sin(\chi) = \mathrm{d}r_b/\mathrm{d}\xi$).

A. Effects of Unit Reynolds Number and Energy Norm

Paredes et al. [12] pointed out that, in order to apply the optimal transient-growth predictions toward transition correlations for nonsimilar boundary-layer flows such as the HLB and TAMU capsules, both the initial and final locations of the transient-growth interval must be varied in addition to the azimuthal wavenumber of the disturbance. First, we address the impact of energy norm (total energy vs. kinetic energy only) on the gain based on outlet energy (Eq. (3)) at $Re/l = 10 \times 10^6$ /m and $\bar{T}_w = 295$ K. The maximum gain within all possible optimization intervals $[\phi_0, \phi_1]$ ($\max_{[\phi_0,\phi_1]} G$) at the corresponding optimal azimuthal wavenumber, $m_{\zeta,opt}$, is plotted for the total energy norm in Fig. 7a and for the kinetic energy norm in Fig. 7b with $J = G^{out}$, respectively. The region included in the figure is limited by the line of zero length optimization interval $\phi_1 = \phi_0$ with $G = 1$ on the diagonal, and a line on the left that delimits the region of the $[\phi_0, \phi_1]$ space that is omitted because the initial disturbance profiles at ϕ_0 peak above the boundary-layer edge and do not exhibit sufficient decay in wall-normal direction (especially the wall-normal velocity component), which in turn prevents the adjoint-based optimization algorithm to converge toward a satisfactory result. However, the excluded portion of the plot is not considered to be important for the present analysis because perturbations with an extended wall-normal support are unlikely to be excited by surface roughness. The maximum disturbance energy gain in the case of J_E^{out} occurs close to the stagnation point (indicated by the black dot), which is in line with the observations for a hemisphere in hypersonic flow [22, 27] and the TAMU capsule with $\bar{T}_w/\bar{T}_e < 1$ [12]. When the norm for the optimization is based on the kinetic energy alone (J_K^{out}), the location of the maximum gain shifts further downstream toward the vicinity of the sonic point as depicted in Fig. 7b ($\phi_{Ma_e=1} \approx 35°$, see also Fig. 4), which again is in close agreement with previous observations for blunt body configurations [12, 22].

From here on, the overall nonmodal growth characteristics of the flow are presented in terms of optimal combination

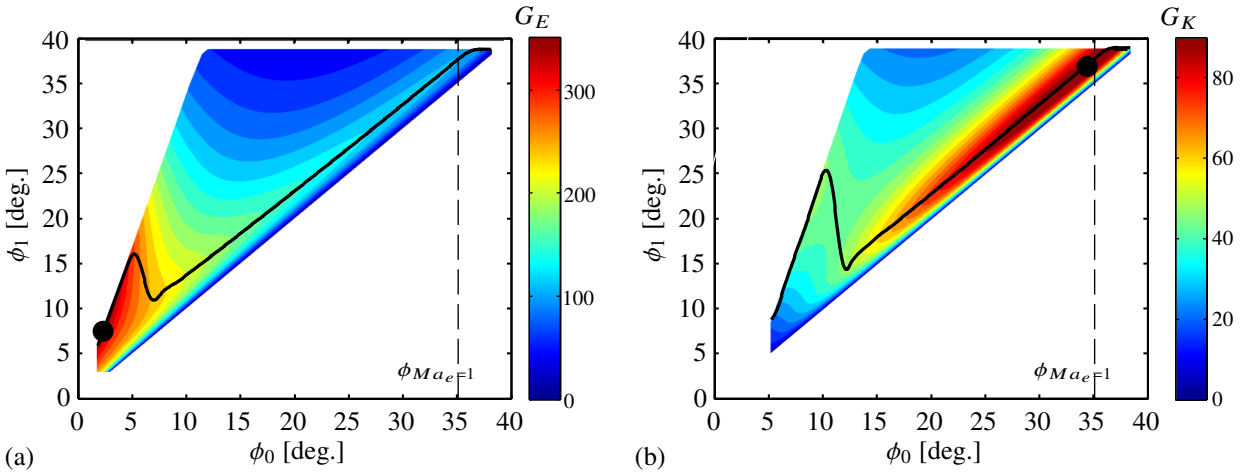

Fig. 7 Isocontours of maximum gain in interval $[\phi_0, \phi_1]$, $\max_{[\phi_0,\phi_1]} G$, and optimal m_ζ for an optimization of (a) total energy gain J_E^{out} and (b) kinetic energy gain J_K^{out}. The black dot indicates the location of the optimal interval where the highest gain occurs, $[\phi_0, \phi_1]_{opt}$. The black line denotes the value of ϕ_1 corresponding to maximum G_E and G_K for a given ϕ_0.

of azimuthal wavenumber, $m_{\zeta,opt}$, and optimal optimization interval length, $[\phi_0, \phi_1]_{opt}$, that lead to the maximum value of the energy gain for a specific initial location. In the following, the impact of unit Reynolds number on the optimal transient-growth characteristics is discussed with respect to objective functions based on outlet energy and mean energy, respectively. The former objective function maximizes the disturbance energy at a prescribed outlet location ϕ_1 (see Eq. (3)), whereas $J = G^{mean}$ maximizes the integral energy in the interval $[\phi_0, \phi_1]$ (see Eq. (4)), which can lead to a higher possible overshoot in the disturbance energy evolution in comparison to $J = G^{out}$.

Figure 8 depicts the evolution of the maximum disturbance energy gain along the angular coordinate for the four possible optimization options (J_E^{out}, J_E^{mean}, J_K^{out}, and J_K^{mean}) at different unit Reynolds numbers and $\bar{T}_w$ = 295 K. Note that the region below $\phi_0 < 6°$ for G_E and $\phi_0 < 11°$ for G_K is omitted, respectively. In those areas, the length of the optimization interval is limited by the boundaries of the parameter space depicted in Fig. 7. In the case of mean energy gain as the objective function for optimization, the length of the optimal optimization interval is much longer than when the objective function corresponds to the outlet energy gain. Therefore, a meaningful comparison of both objective functions with regard to the highest possible disturbance energy gain is not feasible below the mentioned regions. For all cases shown in Fig. 8, maximizing the outlet energy, J^{out}, leads to the highest possible disturbance energy gain within $[\phi_0, \phi_1]_{opt}$ at $m_{\zeta,opt}$. On that account, all of the results presented below to define the upper bound of optimal transient growth for the HLB capsule will pertain only to the objective function based on outlet energy gain ($J = G^{out}$). For all unit Reynolds numbers considered here, the total energy gain of the perturbations reduces with increasing distance from the stagnation point, whereas the kinetic energy gain grows toward the shoulder of the capsule, which in turn implies an increasing share of the overall energy. The sudden decay in energy gain at $\phi_0 \approx 37°$ for both energy norms, G_E and G_K,

is attributed to the shortened optimization interval length at the end of the simulation domain (see Fig. 7).

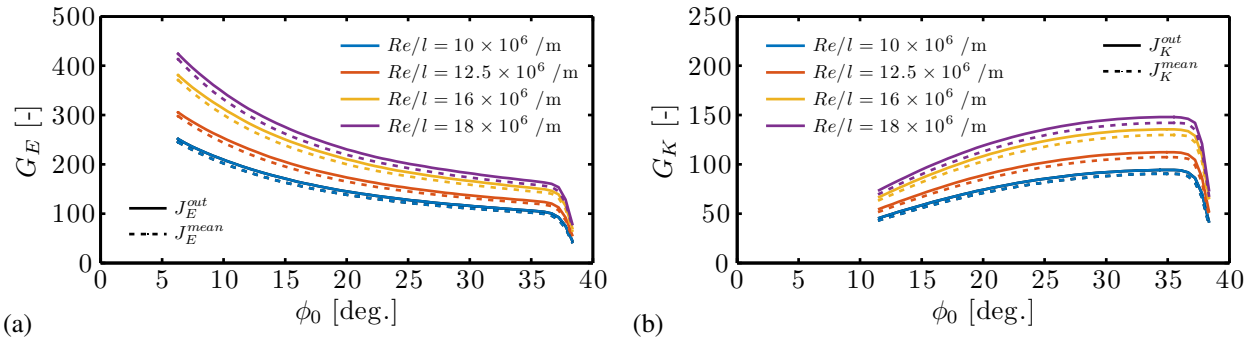

Fig. 8 Streamwise evolution of the maximum optimal disturbance energy gain, $\max_{[\phi_0,\phi_1]} G$, based on outlet energy J^{out} (solid lines) and mean energy J^{mean} (dashed lines) at various unit Reynolds numbers and $\bar{T}_w = 295$ K. The disturbance energy norm is based on (a) total energy and (b) kinetic energy.

From the optimal transient-growth analysis for boundary-layer flows over flat plates, the disturbance energy gain at high Reynolds numbers is known to scale with the body-length Reynolds number Re_L [27, 43]. Figure 9 indicates the nearly linear scaling of the optimal total disturbance energy gain (G_E) with the unit Reynolds number ($Re_R = R \cdot Re/l$). Because the dimension of the body is kept constant when the unit Reynolds number is varied, the observed small deviations from the linear trend are attributed to the differences in the ratio of boundary-layer thickness to the radius of surface curvature. The linear-like unit Reynolds number dependency of the optimal disturbance energy gain is also reported for the TAMU capsule [12].

The transient-growth amplification with regard to the logarithmic amplification ratio, i.e., N-factor, is shown in Fig. 10 in terms of N-factor envelope curves and $\max_{[\phi_0,\phi_1]_{opt}}(N)$. The N-factor based on the total energy norm N_E and kinetic energy norm N_K is defined as

$$N_E(\xi) = 1/2 \ln\left[E(\xi)/E(\xi_0)\right], \quad N_K(\xi) = 1/2 \ln\left[K(\xi)/K(\xi_0)\right]. \tag{10}$$

The vertical dashed lines in Fig. 10 indicate the transition locations for the experiments of Ali et al. [15]. The N-factor at the observed transition location based on the norm for total disturbance energy and kinetic energy are $N_E = 2.54$ and $N_K = 2.45$ at $Re/l = 16 \times 10^6$ /m and $N_E = 2.61$ and $N_K = 2.48$ at $Re/l = 18 \times 10^6$ /m, respectively.

The optimal transient-growth results in Figs. 8–10 have been presented at the optimal parameters of spanwise wavelength and optimization interval. Figure 11a depicts the optimal spanwise wavelength for J_E^{out} in terms of boundary-layer thickness along the initial optimization locations and for four different Reynolds numbers. In addition, the optimal parameters for the TAMU capsule are also plotted at the unit Reynolds numbers from Ref. [12]. For both capsule geometries, the optimal disturbance wavelength displays a good scalability with the boundary-layer thickness. The optimal wavelength with respect to the boundary-layer thickness varies in the range of $(\lambda/\delta)_{opt} \approx [1.6, 2.7]$ for the

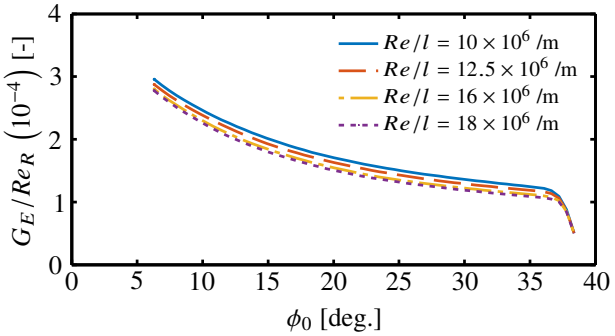

Fig. 9 Impact of unit Reynolds number on the maximum total energy gain, $\max_{[\phi_0,\phi_1]} G_E$, for J_E^{out} and $\bar{T}_w = 295$ K. The energy gain is scaled with the body-length Reynolds number, $Re_R = R \cdot Re/l$.

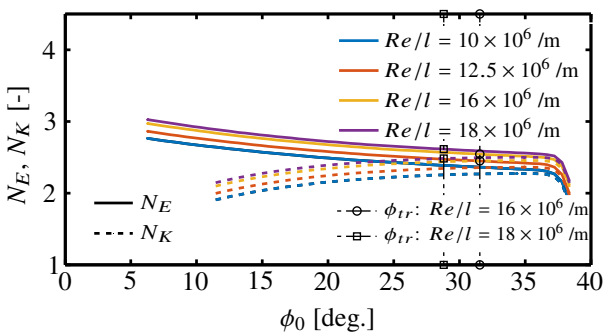

Fig. 10 Impact of unit Reynolds number on the maximum N-factor, $\max_{[\phi_0,\phi_1]} N$, for J^{out} and optimal outlet energy norms based on total and kinetic energy and $\bar{T}_w = 295$ K. The vertical dashed lines mark the transition onset locations based on the experiments of Ali et al. [15]

HLB capsule and $(\lambda/\delta)_{opt} \approx [2.2, 3.0]$ for the TAMU capsule (in the region without domain boundary effects) and is not too different from the findings of Reshotko & Tumin [11] with $(\lambda/\delta)_{opt} \approx [3, 3.5]$ for the flat plate and $(\lambda/\delta)_{opt} \approx 3.2$ for stagnation point flows. Although the predicted optimal wavelengths are similar for both configurations, the small difference may have been caused by the different wall temperatures used in the two studies ($\bar{T}_{w,HLB} = 295$ K, $\bar{T}_{w,TAMU} = 391$ K) and the resulting ratios of wall temperature to boundary-layer edge temperature ($(\bar{T}_w/\bar{T}_e)_{HLB} < 1$ and $(\bar{T}_w/\bar{T}_e)_{TAMU} \approx 1$). The impact of the $\bar{T}_w/\bar{T}_e$-ratio on the optimal parameters for nonmodal disturbance growth will be addressed in the next subsection. Figure 11b shows the length of the optimal transient-growth interval as a function of the initial location for the HLB and TAMU capsules at the respective unit Reynolds numbers. Even though the dimension of the TAMU capsule is only about one half the size of the HLB capsule, the optimal length of the transient-growth interval is nearly the same for both geometries ($(\xi_1 - \xi_0)_{opt} \approx 1.0$ cm) and decreases slightly with the unit Reynolds number. The relatively short optimal optimization length is consistent with the findings of Theiss et al. [17, 18] for the laminar wake flow development behind an isolated roughness element on the forebody of the HLB capsule. The authors have shown that due to the strongly favorable pressure gradient [44], the laminar wake flow experiences growth and decay of the streak amplitude (and also modal disturbance growth) only within a few roughness diameters downstream of the element. Although not shown here, choosing J_E^{out} as the objective function, the boundary layer on both capsule forebodies undergoes optimal nonmodal disturbance growth within 30–40 boundary-layer thicknesses depending on the angular coordinate, which is about fifteen times shorter in comparison to the findings of Reshotko & Tumin [11] for flat plate flows.

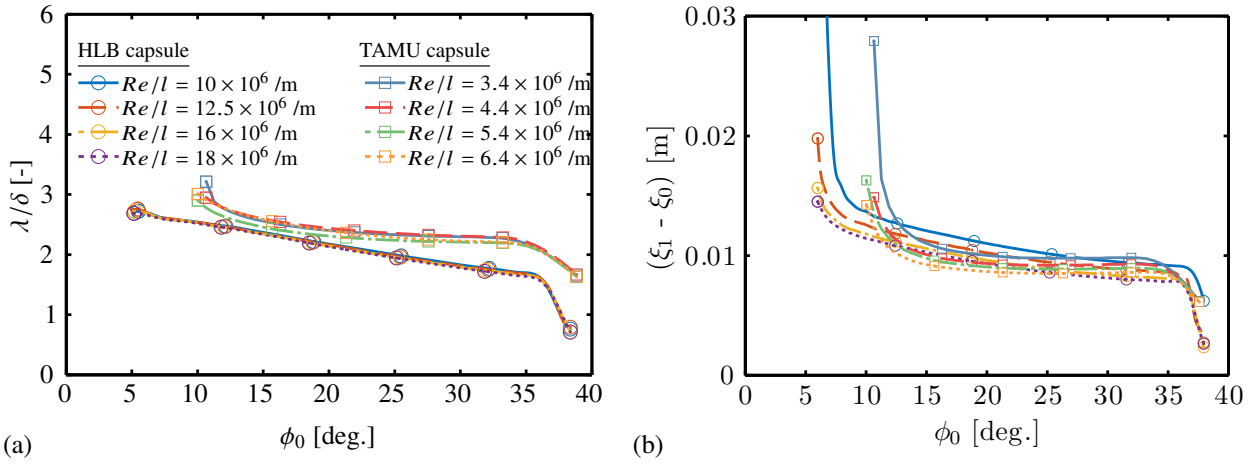

Fig. 11 Impact of unit Reynolds number on optimal optimization parameters for (a) spanwise disturbance wavelength and (b) optimization interval length; ∘: HLB capsule with $\bar{T}_w$ = 295 K, □: TAMU capsule with $\bar{T}_w$ = 391 K. The objective function is J_E^{out}.

B. Effect of Wall Temperature

The effect of the wall temperature on the optimal disturbance growth based on the total and kinetic energy norm is shown in Fig. 12 for both the HLB and TAMU capsules. In accordance with previous findings in the literature [9, 11, 20, 27, 45–47], the disturbance energy gain increases with wall-cooling, whereas the effect is more pronounced in the case of the total energy norm, especially in the vicinity of the stagnation point. The disturbance energy gain based on total and kinetic energy norms is higher for the HLB capsule due to the larger body-length Reynolds number by a factor of about five. The share of the kinetic energy on the total energy of the disturbance increases with $\bar{T}_w/\bar{T}_e$ and for $\bar{T}_w/\bar{T}_e \approx 1$ (HLB capsule: $\bar{T}_w$ = 395 K, TAMU capsule: $\bar{T}_w$ = 391 K; see also Fig. 4) the total energy mainly consists of kinetic energy, i.e., at $\phi_0 = 35.5°$: $G_E = 70.6$, $G_K = 69.7$ for the HLB capsule and $G_E = 10.3$, $G_K = 9.9$ for the TAMU capsule, respectively.

The effect of wall temperature on the optimal spanwise wavelength and the optimal optimization interval for both capsules is shown in Figs. 13a and 13b, respectively. The optimal azimuthal wavelength scaled by the boundary-layer thicknesses decreases slightly with wall cooling for both capsule configurations. The results for the TAMU capsule fall within the range of the HLB capsule data when $(\bar{T}_w/\bar{T}_e)_{TAMU} < 1$. On the other hand, the optimal optimization length increases slightly with wall-cooling ($(\xi_1 - \xi_0)_{opt} \approx 1.1$ cm) along with a higher deviation from the mean value.

C. Revision of Transient-Growth-Based Transition Correlation

Recently, Paredes et al. [12] revisited the distributed roughness-induced transition correlation of Reshotko & Tumin [11], which is the only physics-based model that tackles the blunt-body paradox. The RT-correlation is defined as

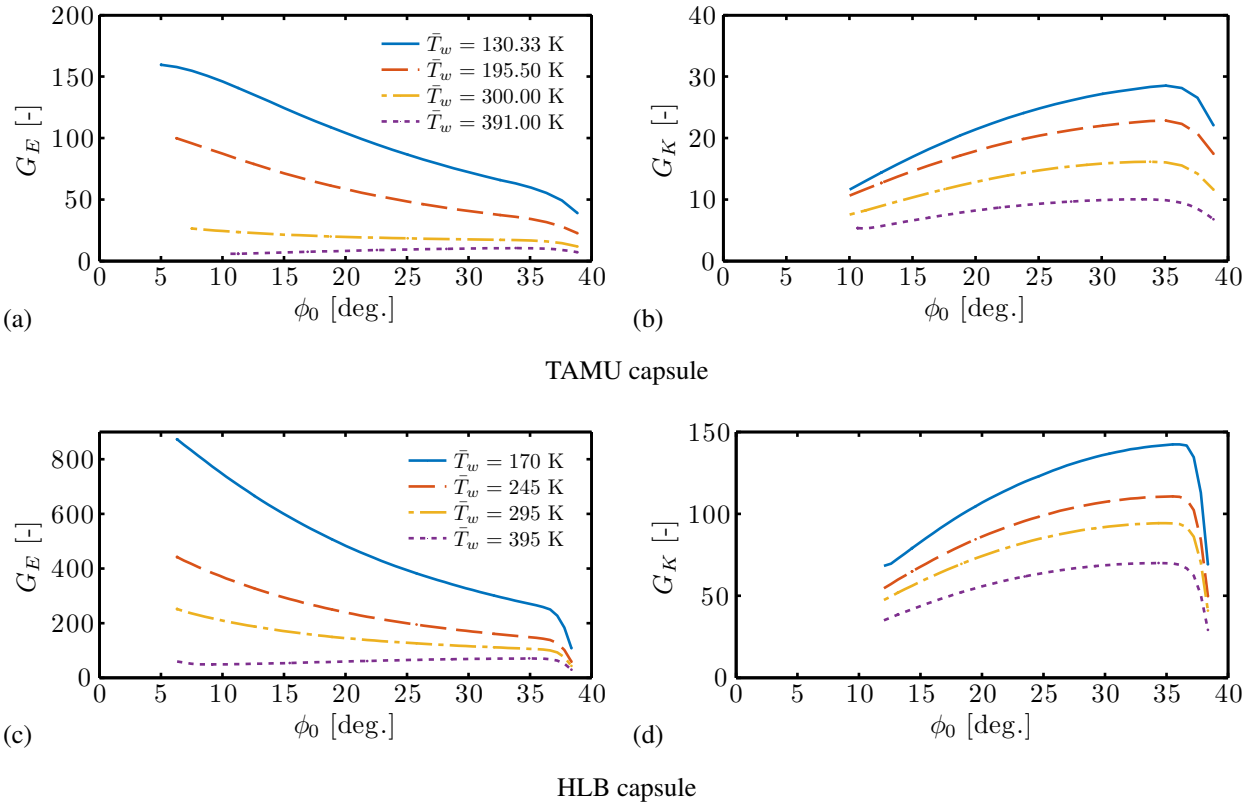

Fig. 12 Streamwise evolution of the maximum optimal disturbance energy gain, $\max_{[\phi_0,\phi_1]} G$, optimized for outlet energy gain at various wall temperatures for (a,b) TAMU capsule, $Re/l = 4.4 \times 10^6$ /m and (c,d) HLB capsule, $Re/l = 10 \times 10^6$ /m. The disturbance energy norm is based on (a,c) total energy and (b,d) kinetic energy.

$$Re_\theta \left(\frac{k}{\theta}\right) \left(\frac{\bar{T}_e}{\bar{T}_w}\right)^{1.27} = 434, \tag{11}$$

where θ denotes the momentum thickness, Re_θ is the Reynolds number based on θ, and k is the roughness height. Reshotko & Tumin [11] assumed that an energy norm at the transition location is related to the roughness-induced energy through the transient-growth energy gain factor G with $E_{tr} = GE_{in}$. Further assumptions are that the input energy scales with $E_{in} = \bar{\rho}_k \bar{u}_k^2$ where the roughness-induced disturbance velocities are proportional to the roughness height, $\bar{u}_k/\bar{u}_e \propto k/\theta$ and the wall-cooling ratio $\bar{T}_e/\bar{T}_w$ is equivalent to $\bar{\rho}_k/\bar{\rho}_e$. As a result, the input energy can be approximated to $E_{in} = \left(\bar{T}_e/\bar{T}_w\right)(k/\theta)^2$. Furthermore, the gain is assumed to scale with the length Reynolds number (as shown in Fig. 9) or with the square of a thickness Reynolds number. Thus, the energy at the transition location results in

$$(E_{tr})^{1/2} = \left(\frac{G^{1/2}}{Re_\theta}\right) Re_\theta \left(\frac{k}{\theta}\right) \left(\frac{\bar{T}_e}{\bar{T}_w}\right)^{0.5}. \tag{12}$$

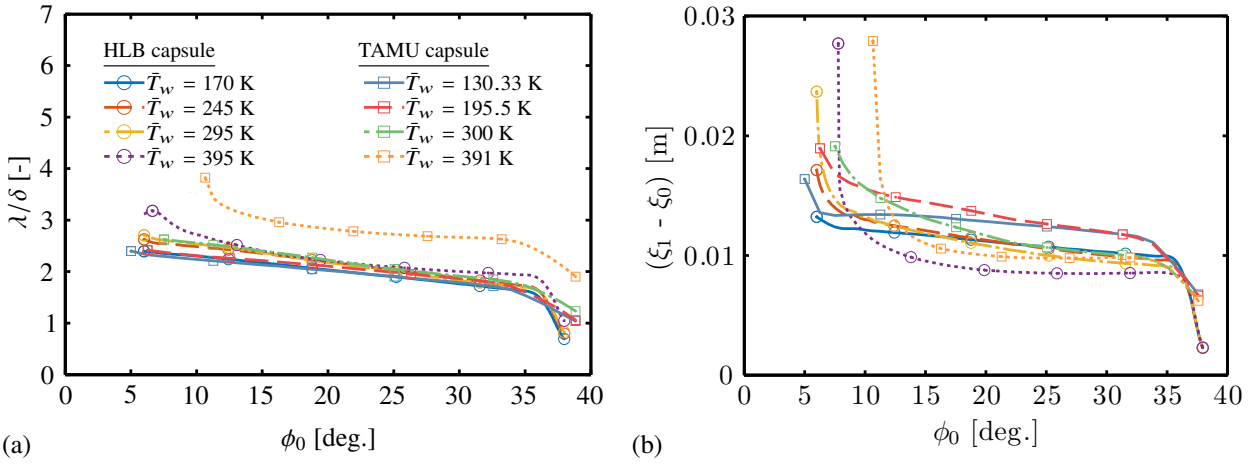

Fig. 13 Impact of wall temperature on optimal optimization parameters for (a) spanwise disturbance wavelength and (b) optimization interval length; ○: HLB capsule with $Re/l = 10 \times 10^6$ /m, □: TAMU capsule with $Re/l = 4.4 \times 10^6$ /m. The objective function is J_E^{out}.

Assuming a power-law variation of the scaled optimum transient energy gain with respect to the surface-to-edge temperature ratio,

$$\left(\frac{G^{1/2}}{Re_\theta}\right) \propto \left(\frac{\bar{T}_w}{\bar{T}_e}\right)^{c_T}, \tag{13}$$

Reshotko & Tumin [9, 11] in the vicinity of $\bar{T}_w/\bar{T}_e \approx 0.5$ obtained a value for the power-law exponent of $c_T = -0.77$, which finally yields Eq. (11). For their analysis they used optimal transient-growth computations based on local, parallel theory and self-similar boundary-layer flow without curvature effects. Furthermore, the initial optimization position and the spanwise wavenumber also remained unchanged. Paredes et al. [12] applied an advanced framework to improve the shortcomings of the optimal transient-growth computations by Reshotko & Tumin [9, 11]; namely, nonlocal transient growth computations including curvature effects for full Navier-Stokes basic state solutions of the TAMU capsule at varying wall temperatures $(\bar{T}_w/\bar{T}_e)_{TAMU} < 1$. The initial ($\xi_{in} = \xi_0$) and final locations ($\xi_{tr} = \xi_1$), as well as the spanwise wavenumber were also optimized. Based on the improved framework, Paredes et al. [12] revised the original RT-correlation and also assumed a power-law variation for the optimum transient energy gain with respect to the surface-to-edge temperature ratio

$$\left(\frac{G^{1/2}}{Re_{\theta_0}}\right)\left(\frac{\bar{\rho}_{e,0}\bar{u}_{e,0}^2}{\bar{\rho}_{e,tr}\bar{u}_{e,tr}^2}\right)^{1/2} \propto \left(\frac{\bar{T}_w}{\bar{T}_{e,0}}\right)^{c_T}. \tag{14}$$

In their analysis, they computed the c_T-value for several possible transition onset locations, ϕ_{tr}, based on the optimal parameter combinations $(\lambda_{opt}, m_{\zeta,opt}, (\phi_{tr} - \phi_0)_{opt})$ for each of the different wall temperatures involved $(\bar{T}_w/\bar{T}_e < 1)$ and for maximizing the total energy gain (J_E^{out}). Moreover, three assumed variations in spanwise disturbance wavelength were also considered. As a result, the set of exponents were nearly insensitive to the assumed λ-variation and all

c_T-values were averaged, resulting in a mean value of $c_T \approx -0.81$, which is remarkably close to the value computed by Reshotko & Tumin [9, 11] based on parallel flow transient-growth calculations. For that reason, the following revised RT-correlation of Paredes et al. [12] only slightly deviates from the originally proposed correlation (Eq. (11))

$$Re_\theta \left(\frac{k}{\theta}\right)\left(\frac{\bar{T}_e}{\bar{T}_w}\right)^{1.31} = 455. \tag{15}$$

The purpose of this section is not to provide an additional transient-growth-based transition correlation, but rather to check if the presented nonmodal growth data for the HLB capsule will result in a similar power-law exponent, c_T, as derived based on the TAMU capsule data. The results shown in Fig. 12a are used to estimate the best-fit exponent through the relation given in Eq. (14). Note, that only results were considered when $\bar{T}_w/\bar{T}_e < 1$, in particular, $\bar{T}_w = 170$ K, 245 K, and 295 K. Figure 14 depicts the variation of the c_T-value at selected transition onset locations. In addition, the results for the TAMU capsule with the spanwise disturbance wavelength variation based on axisymmetric flow (the same assumption as used in this work) are also shown. The angular coordinate for the HLB capsule data is shifted by $\Delta\phi \approx 1.3°$ to match the boundary-layer edge Mach number conditions on the TAMU capsule (see Fig. 4). The averaged power-law exponent for the HLB capsule data is $c_{T,HLB} = -0.813$ and therefore in very good agreement with the equivalent TAMU capsule value of $c_{T,TAMU} = -0.809$.

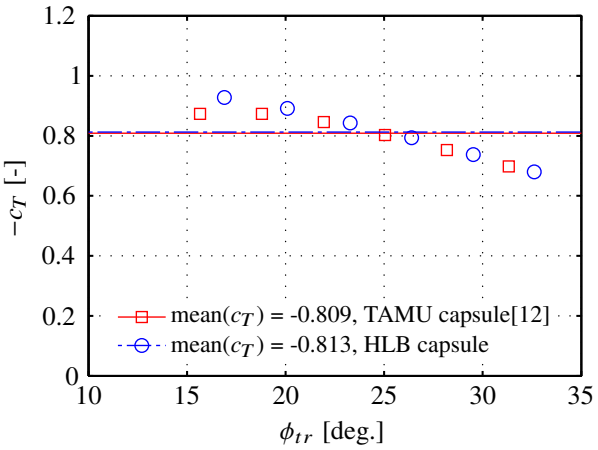

Fig. 14 Best-fit power-law exponent of wall-to-edge temperature ratio for ∘: HLB capsule with $Re/l = 10 \times 10^6$ /m and □: TAMU capsule with $Re/l = 4.4 \times 10^6$ /m.

V. DNS Results for Roughness Patches

To investigate the effect of micron-sized roughness on the capsule boundary layer, direct numerical simulations (DNS) of the supersonic flow around the HLB capsule and the corresponding hemisphere are performed considering finite patches of distributed roughness. The roughness patch geometry for these simulations is deduced from capsule experiments in the HLB [16] and will be quantified subsequently. The generic roughness mimics the Nextel Velvet

Coating that allows for infrared surface temperature measurements and showed to have a distinct influence on transition [8]. The Reynolds number based on the height of the roughness is $Re_{kk} = O(1)$, which is well below the critical value. Thus, immediate transition can be excluded [18, 48]. The possible presence of modal as well as nonmodal growth mechanisms in the roughness wake is investigated in Sec. V.B. Three studies are presented and compared.

Table 1 Freestream conditions for the configurations with rough wall.

Case	Geometry	Ma [−]	p_∞ [Pa]	T_∞ [K]	T_w [K]	Re/l [$1/m$]	AoA [°]
1	HLB Capsule	5.9	478	59	295	$6.25 \cdot 10^6$	24
2	Hemisphere	5.9	478	59	295	$6.25 \cdot 10^6$	0
3	Hemisphere	5.9	1377	59	295	$18.0 \cdot 10^6$	0

Freestream conditions for the different simulations are listed in Table 1. First, the steady flow at $Re/l = 6.25 \times 10^6/\text{m}$ over two different roughness patches located on the HLB capsule is analyzed by RWTH. The computational domain contains capsule, shock wave, and roughness patch. The flow disturbances in the vicinity of the two roughness patches are analyzed and compared. Second, a roughness patch located on the hemisphere from Sec. III.D is investigated by TUM. The wake of the roughness is analyzed for modal instabilities at $Re/l = 18 \times 10^6/\text{m}$, and unsteady DNS imposing pressure disturbances are performed to investigate the interaction of roughness and forced disturbance modes.

A. HLB Capsule Roughness Simulations by RWTH

The roughness patches are located in the center of the spherical forebody of the generic Apollo-like "HLB capsule" in Fig. 3. The origin of the spherical coordinate system is set in the center of the roughness patch, with ξ, ζ, and η being the streamwise, spanwise, and wall-normal direction, respectively. At the given location, the Mach number at the edge of the boundary layer is $Ma_e = 0.5$. For the current Reynolds number $Re/l = 6.25 \times 10^6/\text{m}$, the boundary-layer thickness, displacement thickness, and momentum loss thickness are $\delta = 492\,\mu$m, $\delta^* = 89.2\,\mu$m, and $\theta = 74.3\,\mu$m, respectively. In this section, the boundary-layer edge is defined as the wall normal distance where the flow has 99 % of the total enthalpy of the freestream. The Reynolds number based on the displacement thickness is $Re_{\delta^*} = 109.65$. The roughness patch elements protrude 20 μm into the boundary layer, which is 4% of the boundary-layer thickness and 22% of the displacement thickness. The corresponding roughness Reynolds numbers are $Re_{kk} = 5.82$ and $Re_k = 6.02$, respectively.

The geometry of the aforementioned finite roughness patches is illustrated in Fig. 15, where the flow direction at the boundary-layer edge is from left to right. Each of the patches consists of a certain number of identical single roughness elements having a square base of 100 μm × 100 μm. Two patterns of elements are considered. In Fig. 15a, the "aligned" or "checkerboard" configuration with 5×5 elements is depicted. Based on the flow direction, neighboring elements in the spanwise direction form rows, whereas columns are found in the streamwise direction. This configuration possesses

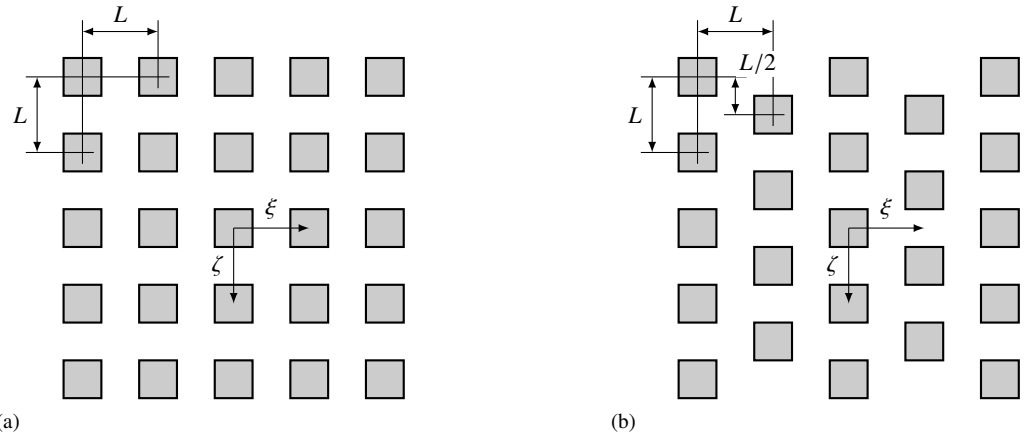

Fig. 15 Roughness setup: a) schematic of the "aligned" distributed roughness having 25 elements; b) schematic of the "staggered" distributed roughness having 23 elements. The elements have a square base of 100μm × 100 μm and a height of 20 μm. The spacing of the elements in both streamwise and spanwise direction is L = 200 μm. The misalignment of the staggered configuration is $L/2$. The flow at the boundary-layer edge is from left to right.

infinite channels between the columns of elements. The spacing between the elements in both streamwise and spanwise direction is $L = 200\,\mu$m. The "staggered" configuration is shown in Fig. 15b. The second and fourth row of elements are reduced by one element and misaligned in the spanwise direction by $L/2$. The projected area in the streamwise direction is gapless. The base area of both patches is $0.9\,\text{mm} \times 0.9\,\text{mm}$.

To resolve the micron-sized roughness patch, the unstructured Cartesian grid is massively refined in the vicinity of the roughness patch. The regions of constant grid resolution around the patch are evidenced in Fig. 16. Note that instead of the single elements of the roughness patch, the hull of the complete patch is depicted. Furthermore, the capsule surface is sketched flat. The gray dashed line in Fig. 16a indicates the surface of the spherical forebody. The Cartesian cell length in the innermost region with the highest resolution is $\Delta d = 1.945\,\mu$m, and it is doubled from region to region. An example of the change in resolution (scaled by a factor of 2) is given at the outermost frame. The streamwise and normal variation of the grid is shown in Fig. 16a, whereas the variation in the ζ-direction is sketched in Fig. 16b. In total, the mesh contains 300×10^6 cells and 30×10^6 cells are clustered in the refined vicinity of the roughness patch.

The streamwise velocity deficit with respect to the smooth configuration u' downstream of the second and third rows of the elements is shown in Fig. 17. In each figure, the staggered and the aligned configurations are shown in the left and right half plane, respectively. Differences between the configurations are restricted to the region close to the wall, i.e., for $\eta < 0.1\,\text{mm}$. Downstream of the staggered second row in Fig. 17a, the highest velocity deficit occurs downstream of the elements slightly above the top of the element at $\eta \approx 30\,\mu$m. Note that it is more intense in the aligned configuration. In the channel between the elements, higher velocities, i.e., a lower velocity deficit, are evident in the aligned configuration. This statement also holds downstream of the identically aligned third row in Fig. 17b. Inside the patch, the difference in

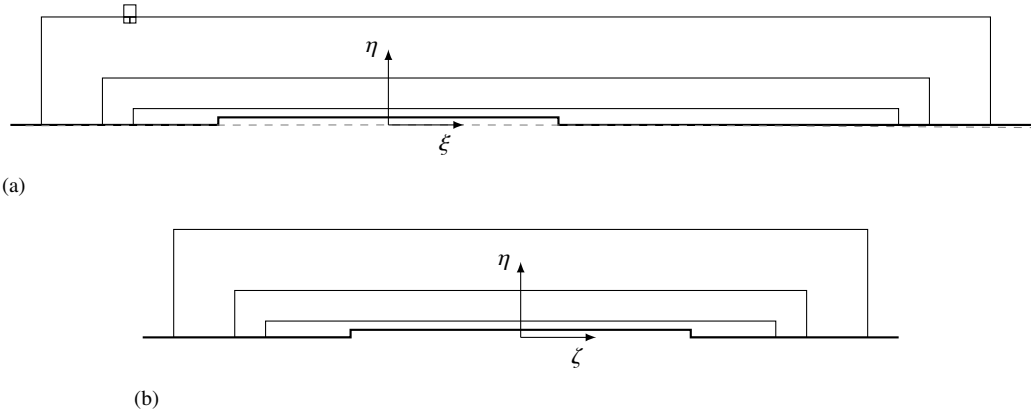

Fig. 16 Grid topology in the vicinity of the roughness patch: a) $\xi - \eta$ plane at $\zeta = 0$, flow at the boundary-layer edge from left to right; b) $\zeta - \eta$ plane at $\xi = 0$. The thick line represents the hull of the roughness patch and the capsule surface. The thin lines indicate a change of grid resolution of the Cartesian mesh, e.g., see upper left corner of (a), where the mesh size scaled by a factor of 2 is indicated.

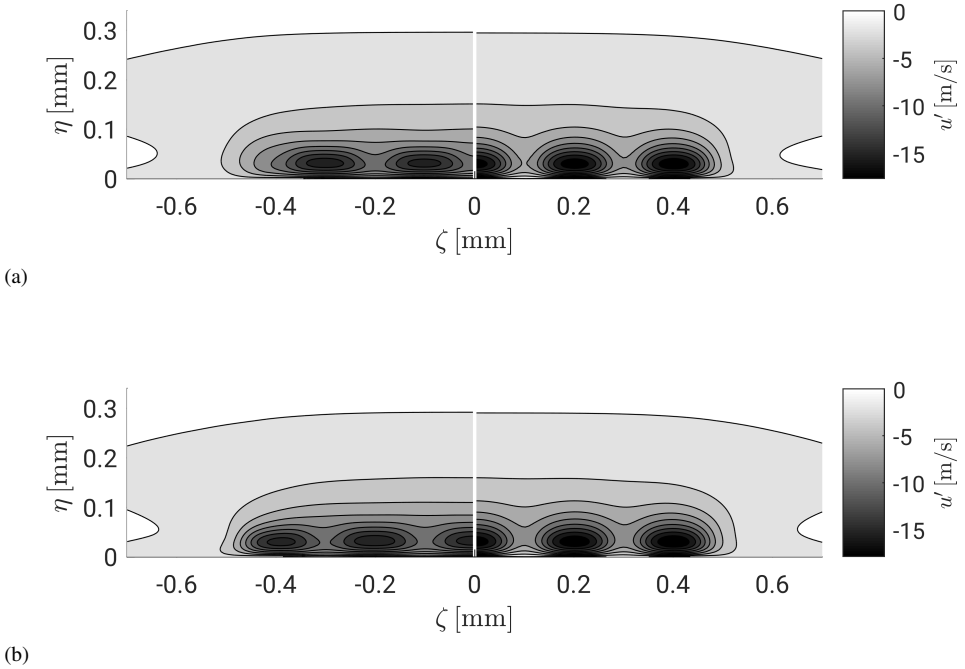

Fig. 17 Streamwise velocity deficit with respect to the smooth configuration u': a) downstream of the second row of elements at $\xi = -L/2 = -100\,\mu$m; b) downstream of the third row of elements at $\xi = L/2 = 100\,\mu$m. The negative half plane shows data of the "staggered" configuration and the positive half plane of the "aligned" configuration.

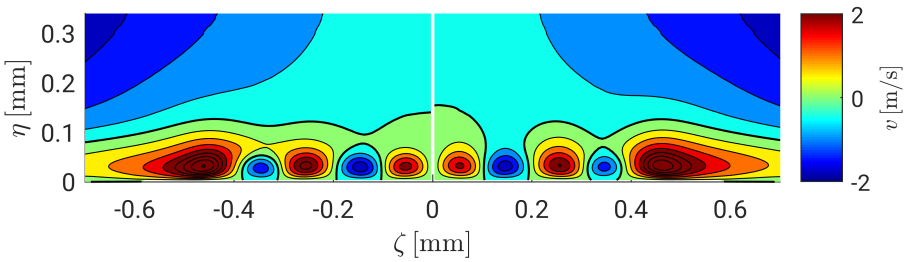

Fig. 18 Velocity in spanwise direction downstream of the last row of elements at $\xi = 2.5\,L = 500\,\mu$m. The negative half plane shows data of the "staggered" configuration, the positive half plane of the "aligned" configuration. For the sake of comparability, the spanwise velocity component of the aligned configuration is multiplied by -1. The thick line indicates $v = 0$.

the streamwise velocity between the flow-channel and the post-element location is higher for the aligned configuration.

The spanwise velocity component normal to the symmetry plane is evidenced in Fig. 18 downstream of the roughness patch. Again, the staggered and aligned roughness elements are compared. The velocity component of the aligned configuration in the positive half-plane is multiplied by -1 to yield a better comparison. The overall pattern for both cases is identical, but the inward flow, i.e., the bright peaks in Fig. 18, is stronger for the staggered configuration. This can be attributed to the inward flow generated by the sum of the elements acting as a finite patch. This discussion is resumed in the subsequent analysis in Sec. V.B on the infinite extent of the rows of roughness elements located on the hemisphere.

B. Hemisphere Roughness Simulations by TUM

The TUM-DNS were carried out on a restricted 3D domain extracted on the hemisphere geometry for $\hat{s} \in [74, 116]$ mm. Details of the restricted domain and the roughness patch are shown in Fig. 5. The roughness patch of the hemisphere consists of 5 squared elements in the streamwise direction. The size of each element and the streamwise spacing are described in Sec. V.A. The patch is centered at $\hat{s} = 77.4$ mm. Dirichlet boundary conditions are applied at the inflow, Riemann invariants are used at the outflow and azimuthal-periodic boundary conditions are used in the spanwise direction. By using periodic boundary conditions, the domain can be limited in spanwise direction to one single roughness periodicity (L). As a result, a considerable reduction of the domain size and, consequently, of computational cost is achieved. The grid of the restricted domain consists of about 29×10^6 points (1320 points in the streamwise and 220 in the wall-normal direction clustered at the roughness location and 100 points equally spaced in the spanwise direction).

1. Steady Simulations

For the case of $Re/l = 6.25 \times 10^6$ /m, we compare the results with the ones presented in Sec. V.A for the HLB capsule configuration. We found that the presence of the roughness on the hemisphere has a similar effect on the flow as

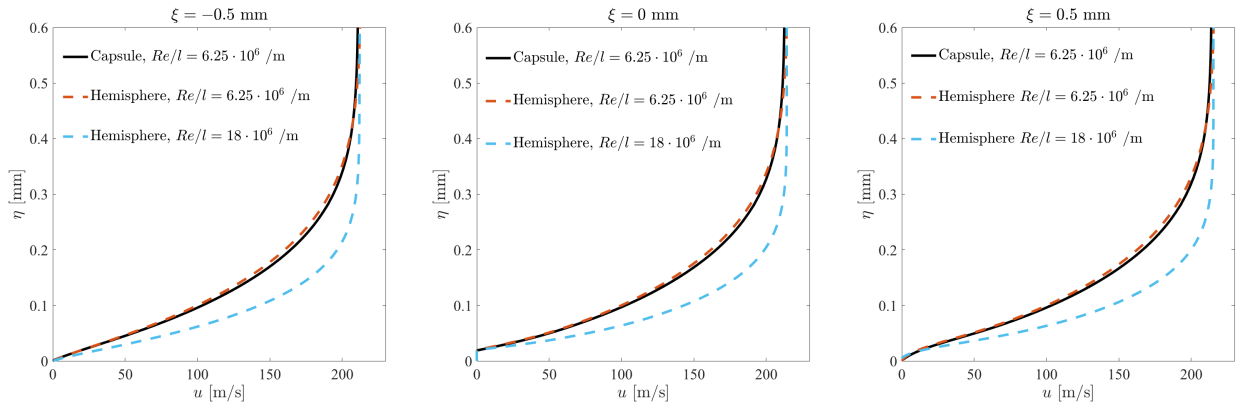

Fig. 19 Comparison of the streamwise velocity profiles of the boundary layer for the hemisphere and the HLB capsule geometry with AoA = 24°. Profiles are extracted at spanwise coordinate $\zeta = 0$ mm. The roughness patch is centered on $\xi = 0$ mm, whereas $\xi = -0.5$ mm and $\xi = 0.5$ mm refer to positions at 0.5 mm before and after the roughness patch, respectively.

in the case of the HLB capsule. In particular, since several roughness elements are present in the spanwise direction in the case of the HLB capsule, the flow in the vicinity of the symmetry plane presents the same periodicity features as in the case of the rough hemispherical geometry. The profiles of the streamwise velocity at three different positions are shown in Fig. 19. A good match can be observed at all three positions. Moreover, Fig. 20 shows a contour map for the spanwise component of the velocity in the $\zeta - \eta$ plane at the position $\xi = 2.5L = 0.5$ mm downstream of the last roughness row. Also in this case, the spanwise velocity data for the hemisphere and the capsule are similar.

Results for the base flow at $Re/l = 18 \times 10^6$ /m are also shown in Fig. 19. Compared to the case with lower unit Reynolds number, a less stable boundary layer is expected; and a higher roughness height to boundary-layer thickness ratio is found, in particular, $k/\delta = 0.069$ and $Re_{kk} = 25$.

Further numerical studies on the hemispherical geometry (not shown here) have been undertaken to investigate the influence of the patch length in the streamwise direction. In fact, compared to the experiments in the HLB, the roughness in the present analysis has a smaller spatial extension. However, we found that further lengthening of the rough region in the streamwise direction, obtained by adding roughness elements upstream of the patch, has a negligible influence on the flow downstream of the patch. Therefore, no significant influence is expected on the stability properties of the wake developing downstream of the last roughness element.

2. Unsteady Simulations

For the case of $Re/l = 18 \times 10^6$ /m, the base flow downstream of the roughness patch has been analyzed with the help of spatial two-dimensional linear stability analysis (LST-2D). The code used to perform LST-2D has already been validated and tested in the case of wake flow instability behind isolated roughness elements [17, 18]. No modal instability could be found in the boundary layer downstream of the roughness patch.

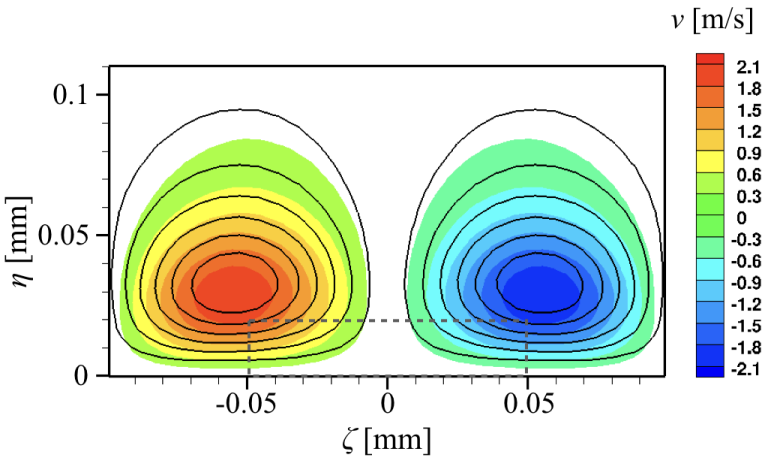

Fig. 20 Contour map for the spanwise velocity at the position $\xi = 2.5, L = 0.5$ mm. Contour lines are used for the capsule results and color shading for the hemisphere results. Contour level spacing is 0.3 m/s. For clarity, the dashed line shows the projection of the roughness elements.

To investigate the presence of possible nonmodal instability mechanisms (i.e., transient growth), time-varying pressure disturbances are introduced at the inflow of the restricted domain (side 2 in Fig. 5) and the development of unsteady disturbances is analyzed by means of unsteady DNS. The disturbance is defined as a superposition of 5 spatial modes with random amplitude A_n and phase ϕ_n,

$$p'(\zeta,\eta) = c(\eta)\cdot\sum_{n=1}^{5} A_n cos\Big(\frac{2\pi n}{\lambda_\zeta}\zeta + \phi_n\Big), \tag{16}$$

where λ_ζ equals the spanwise length of the domain at the inflow position. The function $c(\eta) = e^{-(\eta/\delta)^3}$, with δ being the boundary-layer thickness, guarantees that the perturbation vanishes outside the boundary layer. Experimental investigations at HLB have revealed that relevant frequencies over the rough-wall capsule for large Reynolds numbers lie in the range 100 – 300 kHz [16]. Based on this observation, three different frequencies are investigated in the present analysis: $f_1 = 167$ kHz, $f_2 = 250$ kHz, and $f_3 = 333$ kHz. The resulting inflow condition for the pressure at $\xi = -3.4$ mm is given by:

$$p(\xi_0,\zeta,\eta,t) = \bar{p}(\xi_0,\zeta,\eta) + p'(\zeta,\eta)\sum_{m=1}^{3} cos(2\pi f_m t), \tag{17}$$

where ξ_0 is the streamwise coordinate value of the inflow boundary and $\bar{p}(\xi_0,\zeta,\eta)$ is the pressure distribution of the steady base flow.

Simulations over a long enough time interval corresponding to multiple periods of the forcing field are needed for the transient effects to vanish and we verified the convergence of the spectrum across the entire simulation domain. The

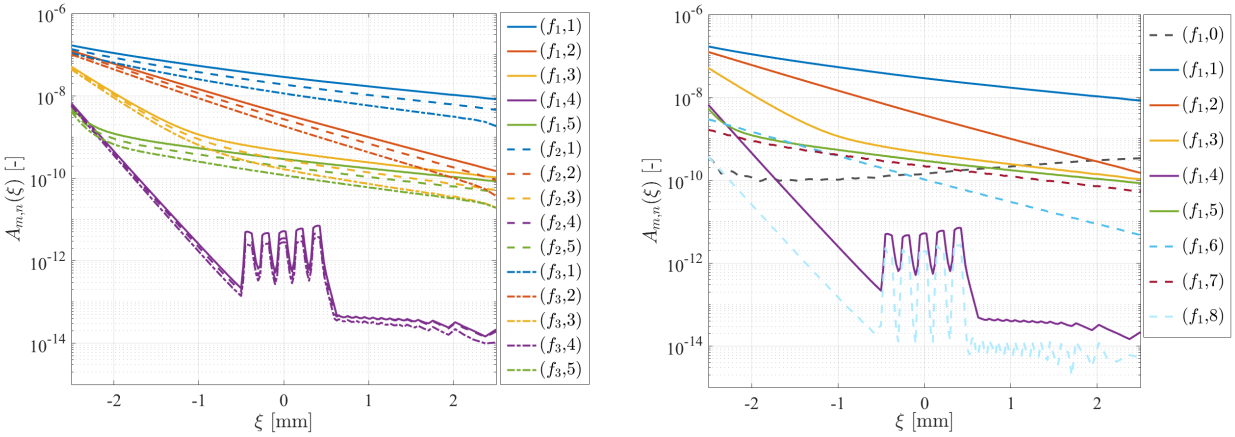

Fig. 21 Evolution of the amplitude of different spatiotemporal Fourier modes along the streamwise coordinate for the streamwise component of the velocity. Values are normalized with the edge velocity at the inflow. The origin of the streamwise coordinate, $\xi = 0$ mm, is set on the center of the roughness patch.

spatiotemporal analysis is conducted by performing a two-dimensional fast Fourier transform (FFT). Any flow variable $g(\xi, \zeta, \eta, t)$ is thus decomposed into spanwise wavenumber-frequency spectra, $G_{m,n}(\xi, \eta)$:

$$g(\xi, \zeta, \eta, t) = \sum_{m=0}^{M-1} \sum_{n=0}^{N-1} G_{m,n}(\xi, \eta) e^{i2\pi(n\zeta/N + mt/M)}, \tag{18}$$

where M and N are the number of time and space samples, respectively. The amplitude $A_{m,n}(\xi)$ of the modes (m, n) is defined as the maximum value of $|G_{m,n}(\xi, \eta)|$ at the position ξ.

Figure 21 shows the amplitude of the perturbed modes with regard to the streamwise component of the velocity as well as the evolution of higher modes for the frequency f_1. Qualitatively similar results are found for the other frequencies and they are not shown here.

As predicted by LST-2D analysis, no amplified modes are found for the analyzed frequencies. In addition, no evidence of possible transient growth could be found for the considered disturbances. Even though a rapid disturbance growth at the roughness location is evident for the modes $(\cdot, 4)$ and $(\cdot, 8)$, their contribution to the total disturbance energy is small.

The absolute value of the time Fourier transform of the streamwise velocity $|\hat{U}_m(\xi, \zeta, \eta)|$ at different streamwise positions is shown in Fig. 22 for $f_1 = 167$ kHz. For clarity, the roughness height and the boundary-layer edge are marked in the figure. At the inflow, the maximum value of the disturbance is found at a height of about $\eta = 0.07$ mm, corresponding to about 0.14δ. Further downstream, viscous effects are responsible for a strong damping of the disturbance in the region close to the wall and the disturbance maximum moves to about $\eta = 0.2$ mm. As the roughness does not produce a significant perturbation at this height, no significant interaction can be observed with the incoming

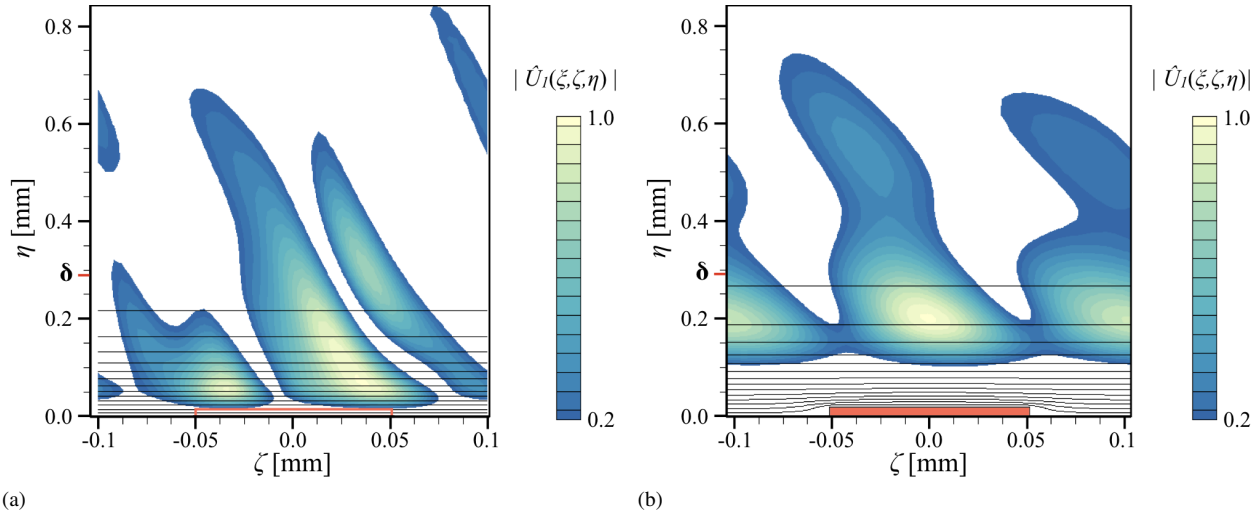

Fig. 22 Time Fourier transform of the streamwise velocity for $f_1 = 167$ kHz: a) at the inflow ($\xi = -3.4$ mm); b) at the roughness position ($\xi = 0$ mm). The absolute values are normalized on a scale of 0 to 1 and values below 0.2 are blanked out. The black isolines indicates the streamwise-velocity distribution and the red line the projection of the roughness element.

unsteady disturbance.

VI. Summary and Conclusions

Optimal transient-growth results for the capsule experiment in the hypersonic Ludwieg tube at the Technische Universität Braunschweig (HLB) at Mach 5.9 were presented and compared with predictions by Paredes et al. [12] for a similar experiment at Mach 6 in the Actively Controlled Expansion (ACE) tunnel at Texas A&M University (TAMU). The angle of attack in the two setups was different, but due to the spherical-segment forebody of both capsule models, the normalized boundary-layer edge data are still very much comparable. In each of the two sets of data, the unit Reynolds number only varied by a factor of about two. Both sets cover a Reynolds number range based on capsule diameter that extends over more than one order of magnitude, however. The maximum gain in energy is higher for the HLB capsule owing to the higher Reynolds numbers but still remains rather moderate in comparison with the amplification factors that correlate the onset of transition in other flows with modal instabilities. Similar trends were observed for the two setups, e.g., concerning the spanwise wavelength normalized by the boundary-layer thickness of the optimal disturbances and the relatively short optimal optimization interval length. In particular, the surface-temperature dependence of the optimal transient-energy gain is very much comparable. Therefore, the value of the power-law exponent of the wall to boundary-layer edge temperature ratio of the correlation for roughness-induced transition that was originally proposed by Reshotko & Tumin [11] and the slightly different value recently derived by Paredes at al. [12] based on optimal transient-growth data for the TAMU capsule are further substantiated by the HLB capsule data at

higher Reynolds numbers.

In some of the HLB experiments, a patch of well-defined micron-sized surface roughness had been applied to the capsule model. The effect of this roughness patch on the boundary-layer flow field was replicated by direct numerical simulations (DNS). A hemisphere geometry has been introduced to reduce the size of the simulation domain and, thus, the computational costs of some of these DNS. We compared the flow on the capsule at angle of attack in the vicinity of the symmetry plane with the one on the hemisphere for both the smooth and the rough-wall geometry and showed that the flow over the hemisphere is similar to the flow over the capsule. In particular, a good match of velocity and temperature profiles is observed.

The stationary disturbance flow field introduced by the well-defined roughness patch was simulated, and its instability characteristics were analyzed. In the case of $Re/l = 18 \times 10^6$ /m where transitional surface heating in the HLB experiment was observed, 2D linear eigenvalue analysis (LST-2D) based on partial differential equations did not reveal any modal instability. Unsteady DNS have been undertaken to investigate possible nonmodal instability mechanisms. Unsteady pressure disturbances are introduced in the domain at three different frequencies (f_1 = 167, 200, and 333 kHz) and a spatiotemporal Fourier analysis has been performed on the entire domain. Neither modal amplification nor transient growth of disturbances could be found. In particular, the height of the roughness elements has been shown to be too small for the roughness wake to amplify the incoming unsteady disturbances.

In summary, we considered several potential mechanisms to explain laminar-turbulent transition on the spherical forebody of blunt reentry capsules. At the conditions of the wind-tunnel experiments, modal disturbances are strongly damped in the boundary layer of the nominally smooth configuration, as shown in Ref. [8]. The complementary studies on the upper limit of nonmodal disturbance growth by using optimal transient-growth theory revealed that the maximum transient gain in energy for stationary disturbances is rather moderate. The maximum transient growth in total energy is found in a relatively short distance downstream of the stagnation point. Roughness-induced transient growth of stationary disturbances is unlikely to serve as the primary cause for the observed onset of transition for the rather low surface-roughness values of the HLB experiment. The direct numerical simulations supplemented by the LST-2D studies on the effects of the roughness patch showed that the modifications of the steady flow field due to the patch are too weak to trigger modal disturbance growth in its wake. Present DNS did not reveal any noteworthy nonmodal disturbance growth in the wake flow. Therefore, a plausible explanation for the observed transition onset in experiment for low surface-roughness values under conditions investigated in the HLB experiment remains to be found and further studies on the interaction of freestream disturbances with small surface roughness are required.

Acknowledgments

Part of this work has been funded by the German Research Foundation (DFG) within the HYPTRANS PAK742. The support is gratefully acknowledged. Computing resources were provided by the High Performance Computing

Center Stuttgart (HLRS), the Jülich Supercomputing Center and the Leibniz Supercomputing Centre Munich (LRZ). The work of the NASA authors was performed jointly under the NASA Transformational Tools and Technologies project and the NASA Hypersonic Technologies Project.

References

[1] Schneider, S. P., "Effects of roughness on hypersonic boundary-layer transition," *J. Spacecr. Rockets*, Vol. 45, No. 2, 2008, pp. 193–209. doi:10.2514/1.29713.

[2] Schneider, S. P., "Summary of hypersonic boundary-layer transition experiments on blunt bodies with roughness," *J. Spacecr. Rockets*, Vol. 45, No. 6, 2008, pp. 1090–1105. doi:10.2514/1.37431.

[3] Reda, D. C., "Review and synthesis of roughness-dominated transition correlations for reentry applications," *J. Spacecr. Rockets*, Vol. 39, No. 2, 2002, pp. 161–167. doi:10.2514/2.3803.

[4] Hollis, B. R., "Correlation of recent and historical rough-wall transition data on hemispherical nosetips," *AIAA Paper 2017-3986*, 2017. doi:10.2514/6.2017-3986.

[5] Johnson, H. B., Candler, G. V., and Wright, M. J., "Boundary layer stability analysis of Mars Science Laboratory aeroshell," *AIAA Paper 2006-0920*, 2006. doi:10.2514/6.2006-920.

[6] Chang, C.-L., Choudhari, M. M., Hollis, B. R., and Li, F., "Transition analysis for the Mars Science Laboratory entry vehicle," *AIAA Paper 2009-4076*, 2009. doi:10.2514/6.2009-4076.

[7] Theiss, A., Lichtmess, M., and Hein, S., "Local stability analysis of laminar-turbulent transition on blunt generic re-entry capsules," *New Results in Numerical and Experimental Fluid Mechanics X, Notes on Numerical Fluid Mechanics and Multidisciplinary Design*, Vol. 132, 2014. doi:10.1007/978-3-319-27279-5_25.

[8] Theiss, A., Hein, S., Heitmann, D., Ali, S. R. C., and Radespiel, R., "Numerical and experimental investigation of laminar-turbulent boundary layer transition on a blunt generic re-entry capsule," *AIAA Paper 2014-2353*, 2014. doi:10.2514/6.2014-2353.

[9] Reshotko, E., and Tumin, A., "The blunt body paradox — A case for transient growth," *Laminar-Turbulent Transition*, Springer, 2000, pp. 403–408. doi:10.1007/978-3-662-03997-7_60.

[10] Schmid, P. J., and Henningson, D. S., *Stability and Transition in Shear Flows*, Springer, 2001. doi:10.1007/978-1-4613-0185-1.

[11] Reshotko, E., and Tumin, A., "Role of transient growth in roughness-induced transition," *AIAA J.*, Vol. 42, No. 4, 2004, pp. 766–770. doi:10.2514/1.9558.

[12] Paredes, P., Choudhari, M. M., and Li, F., "Blunt body paradox and improved application of transient growth framework," *AIAA J.*, (in review).

[13] Leidy, A. N., Reshotko, E., Siddiqui, F., and Bowersox, R. D. W., "Characterizing the transient growth mechanism on a hypersonic blunt body at a high angle of attack," *AIAA Paper 2016-3951*, 2016. doi:10.2514/6.2016-3951.

[14] Leidy, A. N., Reshotko, E., Siddiqui, F., and Bowersox, R. D. W., "Transition due to roughness on blunt capsule: Comparison with transient growth correlation," *J. Spacecr. Rockets*, Vol. 55, No. 1, 2018, pp. 167–180. doi:10.2514/1.a33625.

[15] Ali, S. R. C., Radespiel, R., and Theiss, A., "Transition experiment with a blunt Apollo shape like capsule in hypersonic Ludwieg tube," *63. Deutscher Luft- und Raumfahrtkongress 2014*, Paper 2014-340270, 2014.

[16] Radespiel, R., Ali, S. R. C., Bowersox, R. D. W., Leidy, A. N., Tanno, H., Kirk, L. C., and Reshotko, E., "Experimental investigation of roughness effects on transition on blunt spherical capsule shapes," *AIAA Paper 2018-0059*, 2018. doi: 10.2514/6.2018-0059.

[17] Theiss, A., Hein, S., Ali, S. R. C., and Radespiel, R., "Wake flow instability studies behind discrete roughness elements on a generic re-entry capsule," *AIAA Paper 2016-4382*, 2016. doi:10.2514/6.2016-4382.

[18] Theiss, A., and Hein, S., "Investigation on the wake flow instability behind isolated roughness elements on the forebody of a blunt generic reentry capsule," *Progress in Flight Physics*, edited by D. Knight, Y. Bondar, I. Lipatov, and P. Reijasse, EDP Sciences, 2017. doi:10.1051/eucass/201709451.

[19] Pralits, J., Airiau, C., Hanifi, A., and Henningson, D., "Sensitivity analysis using adjoint parabolized stability equations for compressible flows," *Flow, Turbul. Combust.*, Vol. 65, No. 3–4, 2000, pp. 321–346. doi:10.1023/A:1011434805046.

[20] Tempelmann, D., Hanifi, A., and Henningson, D. S., "Spatial optimal growth in three-dimensional compressible boundary layers," *J. Fluid Mech.*, Vol. 704, 2012, pp. 251–279. doi:10.1017/jfm.2012.235.

[21] Paredes, P., Choudhari, M. M., Li, F., and Chang, C.-L., "Optimal growth in hypersonic boundary layers," *AIAA J.*, Vol. 54, No. 10, 2016, pp. 3050–3061. doi:10.2514/1.j054912.

[22] Paredes, P., Choudhari, M. M., and Li, F., "Blunt-body paradox and transient growth on a hypersonic spherical forebody," *Phys. Rev. Fluids*, Vol. 2, No. 5, 2017, pp. 053903–1–24. doi:10.1103/physrevfluids.2.053903.

[23] Hein, S., Bertolotti, F., Simen, M., Hanifi, A., and Henningson, D., "Linear nonlocal instability analysis - the linear NOLOT code," Tech. Rep. DLR-IB 223-94 A56, 1994.

[24] Chang, C.-L., Malik, M., Erlebacher, G., and Hussaini, M., "Compressible stability of growing boundary layers using parabolized stability equations," *AIAA Paper 91-1636*, 1991. doi:10.2514/6.1991-1636.

[25] Tempelmann, D., Hanifi, A., and Henningson, D. S., "Spatial optimal growth in three-dimensional boundary layers," *J. Fluid Mech.*, Vol. 646, 2010, pp. 5–37. doi:10.1017/s0022112009993260.

[26] Levin, O., and Henningson, D. S., "Exponential vs algebraic growth and transition prediction in boundary layer flow," *Flow, Turbul. Combust.*, Vol. 70, No. 1–4, 2003, pp. 183–210. doi:10.1023/B:APPL.0000004918.05683.46.

[27] Zuccher, S., Tumin, A., and Reshotko, E., "Parabolic approach to optimal perturbations in compressible boundary layers," *J. Fluid Mech.*, Vol. 556, 2006, pp. 189–216. doi:10.1017/s0022112006009451.

[28] Chu, B.-T., "On the energy transfer to small disturbances in fluid flow (Part I)," *Acta Mechanica I*, Vol. 1, No. 3, 1965, pp. 215–234. doi:10.1007/BF01387235.

[29] Mack, L. M., "Boundary Layer Stability Theory," Tech. Rep. JPL Rept. 900-277, Jet Propulsion Lab., California Inst. of Technology, Pasadena, CA, Nov 1969.

[30] Hanifi, A., Schmid, P. J., and Henningson, D. S., "Transient growth in compressible boundary layer flow," *Phys. Fluids*, Vol. 8, No. 3, 1996, pp. 826–837. doi:10.1063/1.868864.

[31] Hermanns, M., and Hernández, J. A., "Stable high-order finite-difference methods based on non-uniform grid point distributions," *Int. J. Num. Meth. Fluids*, Vol. 56, No. 3, 2007, pp. 233–255. doi:10.1002/fld.1510.

[32] Li, F., Choudhari, M. M., Chang, C.-L., and White, J., "Effects of injection on the instability of boundary layers over hypersonic configurations," *Phys. Fluids*, Vol. 25, 2013, pp. 104107–1–15. doi:10.1063/1.4825038.

[33] Hartmann, D., Meinke, M., and Schröder, W., "An adaptive multilevel multigrid formulation for Cartesian hierarchical grid methods," *Comp. Fluids*, Vol. 37, No. 9, 2008, pp. 1103–1125. doi:10.1016/j.compfluid.2007.06.007.

[34] Lintermann, A., Schlimpert, S., Grimmen, J. H., Günther, C., Meinke, M., and Schröder, W., "Massively parallel grid generation on HPC systems," *Comput. Methods Appl. Mech. Engrg.*, Vol. 277, 2014, pp. 131–153. doi:10.1016/j.cma.2014.04.009.

[35] Schneiders, L., Hartmann, D., Meinke, M., and Schröder, W., "An accurate moving boundary formulation in cut-cell methods," *J. Comput. Phys.*, Vol. 235, 2013, pp. 786–809. doi:10.1016/j.jcp.2012.09.038.

[36] Schilden, T., Schröder, W., Ali, S. R. C., Wu, J., Schreyer, A.-M., and Radespiel, R., "Analysis of acoustic and entropy disturbances in a hypersonic wind tunnel," *Phys. Fluids*, Vol. 28, 2016, pp. 056104–1–25. doi:10.1063/1.4948435.

[37] Schilden, T., and Schröder, W., "Numerical analysis of high speed wind tunnel flow disturbance measurements using stagnation point probes," *J. Fluid Mech.*, Vol. 833, 2017, pp. 247–273. doi:10.1017/jfm.2017.674.

[38] Hoarau, Y., Pena, D., Vos, J. B., Charbonnier, D., Gehri, A., Brazak, M., Deloze, T., and Laurendeau, E., "Recent developments of the Navier Stokes Multi Block (NSMB) CFD solver," *AIAA Paper 2016-2056*, 2016. doi:10.2514/6.2016-2056.

[39] Stemmer, C., Birrer, M., and Adams, N. A., "Disturbance development in an obstacle wake in a reacting hypersonic boundary layer," *J. Spacecr. Rockets*, Vol. 54, No. 4, 2017, pp. 945–960. doi:10.2514/1.A33708.

[40] Hollis, B. R., Berger, K. T., Horvath, T. J., Coblish, J. J., Norris, J. D., Lillard, R. P., and Kirk, B. S., "Aeroheating testing and predictions for project Orion crew exploration vehicle," *J. Spacecr. Rockets*, Vol. 46, No. 4, 2009, pp. 766–780. doi:10.2514/1.38579.

[41] Litton, D., Edwards, J., and White, J., "Algorithmic enhancements to the VULCAN Navier-Stokes solver," *AIAA Paper 2003-3979*, 2003. doi:10.2514/6.2003-3979.

[42] Raddatz, J., and Fassbender, J. K., "Block structured Navier-Stokes solver FLOWer," *MEGAFLOW - Numerical Flow Simulation for Aircraft Design*, Springer Berlin Heidelberg, 2005, pp. 27–44. doi:10.1007/3-540-32382-1_2.

[43] Andersson, P., Berggren, M., and Henningson, D. S., "Optimal disturbances and bypass transition in boundary layers," *Phys. Fluids*, Vol. 11, No. 1, 1999, pp. 134–150. doi:10.1063/1.869908.

[44] Theiss, A., Leyh, S., and Hein, S., "Pressure gradient effects on wake flow instabilities behind isolated roughness elements on re-entry capsules," *EUCASS Paper FP-594*, 2017. doi:10.13009/EUCASS2017-594.

[45] Tumin, A., and Reshotko, E., "Spatial theory of optimal disturbances in boundary layers," *Phys. Fluids*, Vol. 13, No. 7, 2001, pp. 2097–2104. doi:10.1063/1.1378070.

[46] Tumin, A., and Reshotko, E., "Optimal disturbances in compressible boundary layers," *AIAA J.*, Vol. 41, No. 12, 2003, pp. 2357–2363. doi:10.2514/2.6860.

[47] Zuccher, S., Shalaev, I., Tumin, A., and Reshotko, E., "Optimal disturbances in the supersonic boundary layer past a sharp cone," *AIAA J.*, Vol. 45, No. 2, 2007, pp. 366–373. doi:10.2514/1.22541.

[48] Klebanoff, P. S., Cleveland, W. G., and Tidstrom, K. D., "On the evolution of a turbulent boundary layer induced by a three-dimensional roughness element," *J. Fluid Mech.*, Vol. 237, 1992, pp. 101–187. doi:10.1017/S0022112092003379.